⌗Fine Structure, Instabilities, and Turbulence in the Lower Atmosphere: High-Resolution In Situ Slant-Path Measurements with the DataHawk UAV and Comparisons with Numerical Modeling

BEN B. BALSLEY[a]

Cooperative Institute for Research in Environment Sciences, University of Colorado Boulder, Boulder, Colorado

DALE A. LAWRENCE

Aerospace Engineering Sciences, University of Colorado Boulder, Boulder, Colorado

DAVID C. FRITTS, LING WANG, AND KAM WAN

GATS, Inc., Boulder, Colorado

JOE WERNE

NWRA, Boulder, Colorado

ABSTRACT

A new platform for high-resolution in situ measurements in the lower troposphere is described and its capabilities are demonstrated. The platform is the small GPS-controlled DataHawk unmanned aerial system (UAS), and measurements were performed under stratified atmospheric conditions at Dugway Proving Ground, Utah, on 11 October 2012. The measurements included spiraling vertical profiles of temperature and horizontal wind vectors, from which the potential temperature θ, mechanical energy dissipation rate ε, Brunt–Väisälä frequency N, temperature structure parameter C_T^2, Thorpe and Ozmidov scales L_T and L_O, and Richardson number Ri were inferred. Profiles of these quantities from $\sim$50 to 400 m reveal apparent gravity wave modulation at larger scales, persistent sheet-and-layer structures at scales of $\sim$30–100 m, and several layers exhibiting significant correlations of large ε, C_T^2, L_T, and small Ri. Smaller-scale flow features suggest local gravity waves and Kelvin–Helmholtz instabilities exhibiting strong correlations, yielding significant vertical displacements and inducing turbulence and mixing at smaller scales. Comparisons of these results with a direct numerical simulation (DNS) of similar multiscale dynamics indicate close agreement between measured and modeled layer character and evolution, small-scale dynamics, and turbulence intensities. In particular, a detailed examination of the potential biases in inferred quantities and/or misinterpretation of the underlying dynamics as a result of the specific DataHawk sampling trajectory is carried out using virtual sampling paths through the DNS and comparing these with the DataHawk measurements.

---

1. Introduction

Many observations have revealed small-scale structures and dynamics extending from the stable boundary layer (SBL) throughout the stable atmosphere. In the troposphere, these dynamics typically include mean winds and shears, gravity waves (GWs) that can occur on a wide range of scales and account for the major vertical fluxes of energy and momentum (e.g., Gossard and Hooke 1975; Sun et al. 2004; Stull 2012; Nappo 2013), and various instabilities arising from GWs and/or wind shears achieving large amplitudes. The latter include Kelvin–Helmholtz instabilities (KHI), wave–wave interactions, GW breaking, intrusions, and the transitional dynamics leading to turbulence (e.g., Fritts and Rastogi 1985; Fritts et al. 2016).

These dynamics play central roles in the evolution of the atmosphere and its prediction. Hence, a better understanding of these dynamics is important, and

---

⌗ Denotes content that is immediately available upon publication as open access.

---

[a] Deceased.

Corresponding author: Dale Lawrence, dale.lawrence@colorado.edu

improved measurement capabilities are essential to achieving this goal. In the lower troposphere, sensors on towers, aboard research aircraft, and suspended below balloons and kites have enabled many valuable measurements to date. Sensors enabling vertical profiling, in particular, have demonstrated ubiquitous small-scale structure in the velocity, temperature, tracer, and turbulence fields that are believed to play key roles in the structure and evolution of the atmospheric state.

These small-scale structures often manifest as thin, sharp gradients in horizontal wind, potential temperature, and/or tracers separated by thicker layers having much weaker gradients, which we will refer to as "sheet and layer" (S&L) structures. Numerical modeling of multiscale dynamics involving superposed mean and GW motions reveals that such S&L structures arise naturally and include local GW breaking, KHI, intrusions, and local turbulence events (Fritts et al. 2013, 2016). Similarities in these multiscale dynamics throughout the atmosphere are striking, though the spatial scales vary dramatically because of the exponential increase in kinematic viscosity and the implied decrease in Reynolds number for dynamics at the same scales at higher altitudes. The lower troposphere is thus a natural laboratory for small-scale dynamics studies having broad relevance throughout the atmosphere. It is also a region that is far more easily, economically, and quantitatively studied than higher altitudes because of technologies enabling multiple, simultaneous, continuous, and/or repeated measurements in a common volume.

Comprehensive, multi-instrument dynamics studies in different environments include the 1999 Cooperative Atmosphere–Surface Exchange Study (CASES-99) performed in Kansas (Poulos et al. 2002), the Vertical Transport and Mixing (VTMX) experiment performed in Utah in 2000 (Doran et al. 2002), the Meteor Crater Experiment (METCRAX) performed in the Arizona Meteor Crater in 2006 (Whiteman et al. 2008), and the Mountain Terrain Atmospheric Modeling and Observations (MATERHORN) campaign (Fernando et al. 2015) also performed in Utah in 2012 and 2013. These experiments, and additional measurements using similar instrumentation at other sites, have quantified diverse lower atmosphere structures and dynamics to a degree not possible without high-resolution profiling. Specific examples include the following:

1) the presence of layered structures in temperatures and horizontal winds suggestive of small vertical wavelength GWs or remnants of previous mixing events (e.g., Gossard et al. 1985; Balsley et al. 1998, 2003, 2006; Muschinski and Wode 1998; Mahrt 1999; Doran et al. 2002; Sorbjan and Balsley 2008; Whiteman et al. 2008)

2) in situ measurements of the temperature structure parameter C_T^2 and mechanical energy dissipation rate ε (e.g., Balsley et al. 2006, 2012)

3) strong layering in radar reflectivity believed to result from temperature sheets having high C_T^2 (e.g., Gossard et al. 1985; Eaton et al. 1995; Muschinski et al. 1999; Sun et al. 2004)

4) measurements of dynamics leading to instabilities and turbulence, for example, strong nocturnal boundary layer jets, GWs, solitary waves, density currents, intrusions, and seiches (e.g., Mahrt 1985; Blumen et al. 2001; Balsley et al. 2002; Grimshaw 2002; Fritts et al. 2003a; Newsom and Banta 2003; Sun et al. 2002, 2004; Meillier et al. 2008; Whiteman et al. 2008)

The instrument capabilities noted above have yielded significant advances in our understanding of these S&L dynamics over many years. In most cases, however, they have been limited in vertical resolution, altitude extent, temporal resolution of the same air volume, or measurement dexterity because of fixed instruments or high costs. New small unmanned aerial systems (UAS) provide the ability to address these deficiencies in several ways (Balsley et al. 2012; Lawrence and Balsley 2013a). These include 1) rapid, successive sampling of the same air volume; 2) flight paths designed to address specific dynamics targets tracked in real time; 3) the ability to sample multiple environments in a common campaign; and 4) a capability for sampling by multiple coordinated UASs in the same air volume. We believe guidance of modeling efforts by these new high-resolution measurements offer tremendous potential for advancing our understanding of not just the forms and statistics of these fields but also the dynamics driving their structures and evolutions.

Here, we describe the DataHawk UAS measurement capabilities and measurements performed at Dugway Proving Ground (DPG) in October 2012. The objective was to explore instability and turbulence dynamics using coincident, high-resolution, in situ temperature and wind sensors. The DataHawk was under global positioning system (GPS) control, using a custom autopilot developed at the University of Colorado, and flew successive ascending and descending helical profiles at various ascent/descent rates and helix diameters, sampling the evolution of the environment over a 5-h interval on the morning of 11 October. The measurements yielded a number of results, suggesting local instability and/or turbulence events and evidence of evolving S&L

structures. We describe several of these events in this paper, employing high-resolution numerical modeling to aid our interpretations. We also address important questions about the potential biases that can arise with any in situ UAS sampling strategy. The measurements and analysis methods are described in section 2. Analyses of the measurements and parallel numerical modeling are presented in sections 3 and 4. A discussion of these results in the context of previous measurements and modeling is provided in section 5. Our conclusions are presented in section 6.

2. Measurements and analysis methods

The DataHawk (Lawrence and Balsley 2013a) provides a platform for in situ sensing in large volumes, constrained only by the flight limitations imposed by a fixed-wing vehicle (see Fig. 1). Typically, the flight speed is $\sim 14 \, \text{m s}^{-1}$ when climbing or descending at relatively small rates. Instead of common waypoint navigation schemes, the DataHawk utilizes vector field guidance laws (Lawrence et al. 2008) that attract the vehicle to horizontal motion on a circle, with constant climb and descent rates between $\pm 2 \, \text{m s}^{-1}$. This enables a variety of smooth measurement trajectories to be specified with a simple flight planning process, as opposed to large numbers of waypoints required to obtain similar results with waypoint-based guidance schemes, for example, for altitude variation or sampling on large circles. The smallest practical circle diameter is 100 m, but much larger circles were used to collect the data described here. In addition, the DataHawk utilizes an autonomous launch and landing capability that obviates a trained remote control (RC) pilot for normal operations. Otherwise, the DataHawk vehicle is similar to other small UAS in basic capabilities, such as flight speed, duration, etc., as described in Reuder et al. (2012) and Lawrence and Balsley (2013a). However, it does carry a unique high-resolution "coldwire" temperature sensor, as described below.

a. Direct measurements

Measurement locations were obtained using a single-frequency GPS receiver (u-blox LEA-6) without augmentation [carrier phase, Wide Area Augmentation System (WAAS), real-time kinematic (RTK), etc.], reported at 5 Hz. This typically provides locations within 10-m error laterally with drift rates that are slow compared to lateral motions, making this low-cost solution entirely adequate for the atmospheric measurements of interest. However, vertical solutions have episodes of variation that are significant compared to lateral motions, necessitating improved altitude estimates. This is
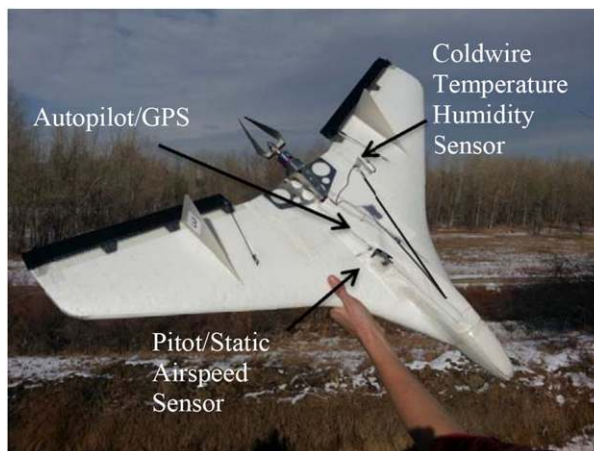

FIG. 1. DataHawk UAS showing the location of main sensing elements. Airframe mass is 700 g and wingspan is 1 m.

obtained using pressure altitude computed from the *U.S. Standard Atmosphere* model (COESA 1976):

$$h = 44\,330[1 - (P/1013.25)^{0.190\,284}]$$

where altitude h is in meters above mean sea level (m MSL) and absolute pressure P is in millibars (mb). Although this provides smooth, high-resolution estimates, they are not accurate over large altitude variations and long periods due to slow changes in the bulk atmosphere properties used in the model (nominal temperature and pressure, local lapse rate). Large-scale accuracy is improved by fitting pressure altitude to GPS altitude with a third-order polynomial in postflight analysis, taking advantage of the smaller bounds on long-term GPS drift. Absolute pressure P is provided by a Measurement Specialties MS5611 sensor with a resolution of 0.012 mb, providing an altitude resolution of 5.4 cm at 1 km MSL. Resulting corrected pressure altitudes agree with GPS altitudes within 20-m error over the altitude ranges obtained here.

Onboard sensors directly measured temperature and airspeed. Temperature was measured in two ways. A Texas Instruments ADS1118 provides a slow but calibrated reference (5-s time constant, $\pm 1°\text{C}$ from $-40°$ to $125°\text{C}$, with $0.03°\text{C}$ resolution), reported at 10 Hz. Higher bandwidth and resolution temperature were also measured with a 0.6-ms time constant using a custom coldwire resistance temperature detector, based on the Tethered Lifting System sensor (Frehlich et al. 2003), but miniaturized for small UAS use and integrated with the University of Colorado (CU) autopilot. The resulting sensor is small enough (10 g) to be used on virtually any UAS (see Fig. 1). It consists of a 5-μm-diameter platinum wire excited with a constant 1-mA

current. The voltage across the wire is amplified, anti-aliased, and 16-bit digitized at 80 Hz, providing a resolution of 0.003°C and a range of −60° to +40°C. This temperature-dependent voltage has an offset and scale factor that is highly dependent on the platinum wire length, and this is difficult to control precisely in the custom manufacturing process that hand solders Ag–Pt Wollaston wire to prongs and, subsequently, etches the Ag cladding away. Wires are assembled/etched in batches of five, at an effective unit cost of $5.00. Although commercially produced wire assemblies are available, they are about 10 times larger, 20 times more expensive, and individual calibration is still needed. To eliminate wire resistance and electronics offset and gain errors, we employ a postflight calibration that fits cold-wire voltage to the (slower) ADS1118 sensor using a first-order polynomial to determine the uncertain offset and scale factor for each wire. Flights discussed here typically had bulk temperature variations of 4°C over 400 m of altitude change. The reference sensor in this calibration could have an offset error as much as ±1°C and a scale factor error of ±1.2%. Platinum wire temperature coefficient of resistance changes very slowly with temperature (on the order of 0.4% °C^{-1}), making the measured wire voltage quite linear with temperature over a 4°C range, enabling first-order polynomial calibration curves from coldwire voltage to temperature. Absolute temperature has no bearing on the results of this paper, so the offset errors in this calibration are not important. The focus is on fluctuations, and these can have scale factor errors less than 5%.

Airspeed is provided by a custom pitot-static tube and Freescale MPXV7002 differential pressure sensor, also amplified and digitized at 80-Hz, providing a resolution of 0.008 m s^{-1} and a range of 0–30 m s^{-1}. The dynamic pressure P in pascals (Pa) in this measurement is related to the airspeed in meters per second (m s^{-1}) by

$$v_a = \sqrt{(P - P_o)/(\rho c_a)},$$

where ρ is the air density (kg m^{-3}). The offset in this measurement is calibrated in preflight procedures at zero airspeed, and the median GPS speed over a circular orbit is used in postflight calibration to precisely adjust the airspeed scale factor: GPS (ground) speed v_g is the magnitude of the vector sum of wind v_w and relative wind v_a (airspeed), so on a circle $v_g \in [v_a - v_w, v_a + v_w]$ whose median is v_a. During a steady ascent or descent (as executed in the flights described herein), the mean airspeed (i.e., not including turbulent fluctuations) is essentially constant; hence, c_a is adjusted to make the mean v_a agree with the median of GPS speeds averaged over several circles. Altitude variation in ρ is accommodated by

calculating it as a function of measured barometric pressure and temperature using the (dry) *U.S. Standard Atmosphere* model. The DataHawk carries a relative humidity sensor, but the effects of water vapor on density are small and were not incorporated. Note that this calibration method also accommodates mean airspeed errors resulting from the location of the pitot sensor at its protected location behind the nose and on top of the DataHawk airframe (see Fig. 1).

b. Derived quantities

Horizontal winds were derived by a local estimation algorithm that determined the mean wind vector that was consistent with measured GPS velocity and pitot airspeed over 10-s intervals (Lawrence and Balsley 2013b). Since airspeed is essentially constant, this algorithm fits a circle of relative wind vector magnitude (constant airspeed) to the triangle that sums wind vectors and measured GPS velocity vectors to equal relative wind vectors. Repeating this 10 s later produces another circle, and the intersection of these two circles produces two solutions for the wind vector, one of which is unrealistically large. In the flights considered here, this estimate effectively averages the winds over a horizontal distance of about 50 m and a vertical distance of 1 m. Accuracy of this wind-finding approach has been analyzed in detail (see the appendix). This results in maximum errors in instantaneous wind estimates ranging from 0.6 to 1.5 m s^{-1} along the circular path. The resulting wind data are presented (see Fig. 6 below). Note that the wind data are free of obvious correlations with the vehicle location on the circle (which also correlates with vehicle deviations from a steady banked flight in wind). The ability to see motion-correlated artifacts is one of the main reasons for presenting data in the format shown (Fig. 6).

Several other useful derived parameters were obtained to assist in interpreting the measurements. These parameters were estimated by averaging over time intervals I_a that range from 1 to 16.7 s, in order to examine behavior over a range of resolutions, as noted below.

Potential temperature θ at each altitude h is obtained from calibrated coldwire temperature T (K) using the *U.S. Standard Atmosphere* adiabatic lapse rate L, and referencing θ to T at the floor h_f of each vertical profile as

$$\theta = T[1 - L(h - h_f)/T]^{-g/LC_p},$$

where g is the gravitational acceleration and C_P is the constant-pressure specific heat.

Thorpe displacements d' represent the distance that air parcels are out of place vertically, relative to a quiescent, stably-stratified atmosphere. At each altitude d' are obtained by first sorting θ into a monotonically

increasing (stably stratified) sequence θ_s above h_f, then computing the altitude difference between the sorted and unsorted parcels. The related Thorpe scale (Thorpe 1977) is defined as $L_T = <d'^2>^{1/2}$, where the angle brackets ($<>$) represent an average over a suitable interval, here chosen to be a $3 I_a$ time interval. At the ascent/descent rates of about $0.3\,\mathrm{m\,s^{-1}}$ here, this results in vertical averages in L_T ranging from 0.3 to 5 m.

The local buoyancy frequency N is estimated from $N^2 = (g/\theta_s)\,d\theta_s/dz$; here, θ_s is averaged over the same $3 I_a$ time intervals.

The temperature structure turbulence parameter is computed using the method of Frehlich et al. (2003), where high-rate coldwire temperatures are processed using a spectral fitting procedure. For the ith record of I_a seconds of coldwire data $T_i(n\Delta t)$ (K), the data are linearly detrended and tapered with a Hanning window to reduce spectral artifacts. These records are processed using a conventional fast Fourier transform (FFT) and normalized to yield true spectral amplitudes A_T (K), considering only frequencies up to the Nyquist rate, that is,

$$A_T(m\Delta f) = \frac{2}{N}\sum_{n=0}^{N-1} T_i(n\Delta t)e^{\frac{-j2\pi mn}{N}},$$

where m is the frequency index and n is the time index.

The corresponding power spectral density is given by $P_T(m\Delta f) = (I_a/2)|A_T(m\Delta f)|^2$ ($\mathrm{K^2\,Hz^{-1}}$) and should have the form $P_T(m\Delta f) = aU_i^{2/3}C_T^2(m\Delta f)^{-5/3}$ in the inertial subrange, where $a = 0.073\,084\,6$ and U_i is the mean airspeed over the ith I_a time record ($\mathrm{m\,s^{-1}}$). The term U_i in this expression serves to convert temporal frequency to spatial wavenumber, based on the assumption of a Taylor frozen turbulence hypothesis. Since the spectral data are noisy, an estimate for the spectral amplitude $s_T = aU_i^{2/3}C_T^2$ is found by weighting $P_T(m\Delta f)$ by $(m\Delta f)^{-5/3}$ and then finding the least squares fit of the weighed spectrum to a constant function of frequency over a suitable frequency interval. The frequency interval should lie within the inertial subrange, should be free of periodic artifacts caused by DataHawk motions and electronic interference, and should not extend into frequencies where the electronic noise floor causes a departure from the Kolomogorov $f^{-5/3}$ characteristic. Here, we use a frequency interval of 4–40 Hz. The resulting function value s_T is then used to solve for $C_T^2 = s_T/(0.073\,084\,U_i^{2/3})$ on the ith I_a time record. Figure 2 shows a typical spectrum and the fitted estimate $s_T f^{-5/3}$ used to derive C_T^2 for that time interval.

A similar spectral fitting procedure yields local estimates of the turbulent ε by processing airspeed data. Although relative velocity is a vector quantity, estimation of ε using only the longitudinal aircraft component
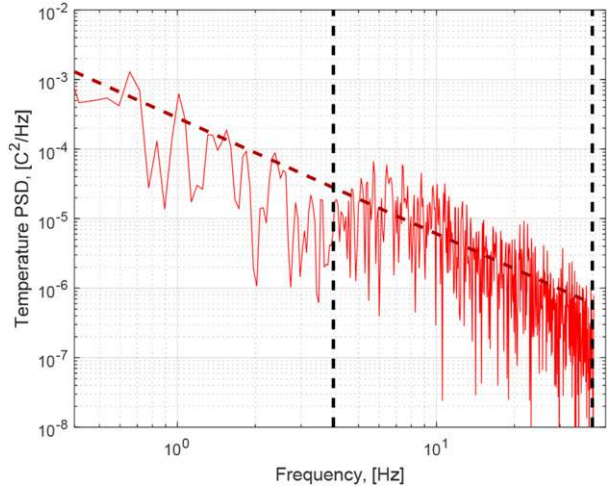

FIG. 2. Typical power spectral density of temperature, showing the fit $f^{-5/3}$ characteristic (red dashed line) and the 4–40-Hz frequency interval used for the least squares fit (black dashed lines).

measured by the pitot-static sensor is justified on the basis of isotropy in stratified flows as noted in Frehlich et al. (2003), provided the buoyancy Reynolds numbers Re_b (defined below) are larger than 100. Figure 3–5 show Re_b to be larger than 1000 throughout the flights discussed here. The same 4–40-Hz frequency interval was used for least squares estimation of the spectral $f^{-5/3}$ characteristic. In this case the weighted function value s_V is related to ε by $\varepsilon = (s_V/0.146\,169)^{3/2}/U_i$. See Frehlich et al. (2003) for additional background on these spectral methods.

Given ε, N, and kinematic viscosity ν, the Ozmidov scale, Kolmogorov scale, and buoyancy Reynolds number are defined as $L_O = (\varepsilon/N^3)^{1/2}$, $L_K = (\nu^3/\varepsilon)^{1/4}$, and $\mathrm{Re}_b = \varepsilon/(\nu N^2) = (L_O/L_K)^{4/3}$, respectively. Finally, the local Richardson number is defined in terms of the local horizontal wind u and N as $\mathrm{Ri} = N^2/(du_h/dz)^2$. To prevent errors from residual small-scale wind-finding variations from corrupting the (gradient) Richardson number in Figs. 3–5, wind data are smoothed with a 200-s time constant filter (see plots of U and V), that averages over a spatial scale that is approximately one complete circle. The terms L_O and L_T are assessed because they are believed to be proportional with some spatial averaging, allowing measured L_T to yield an estimate of ε using the abovementioned relations (e.g., Clayson and Kantha 2008; Fritts et al. 2016).

3. Measurement results

a. DataHawk vertical profiles of measured and inferred quantities

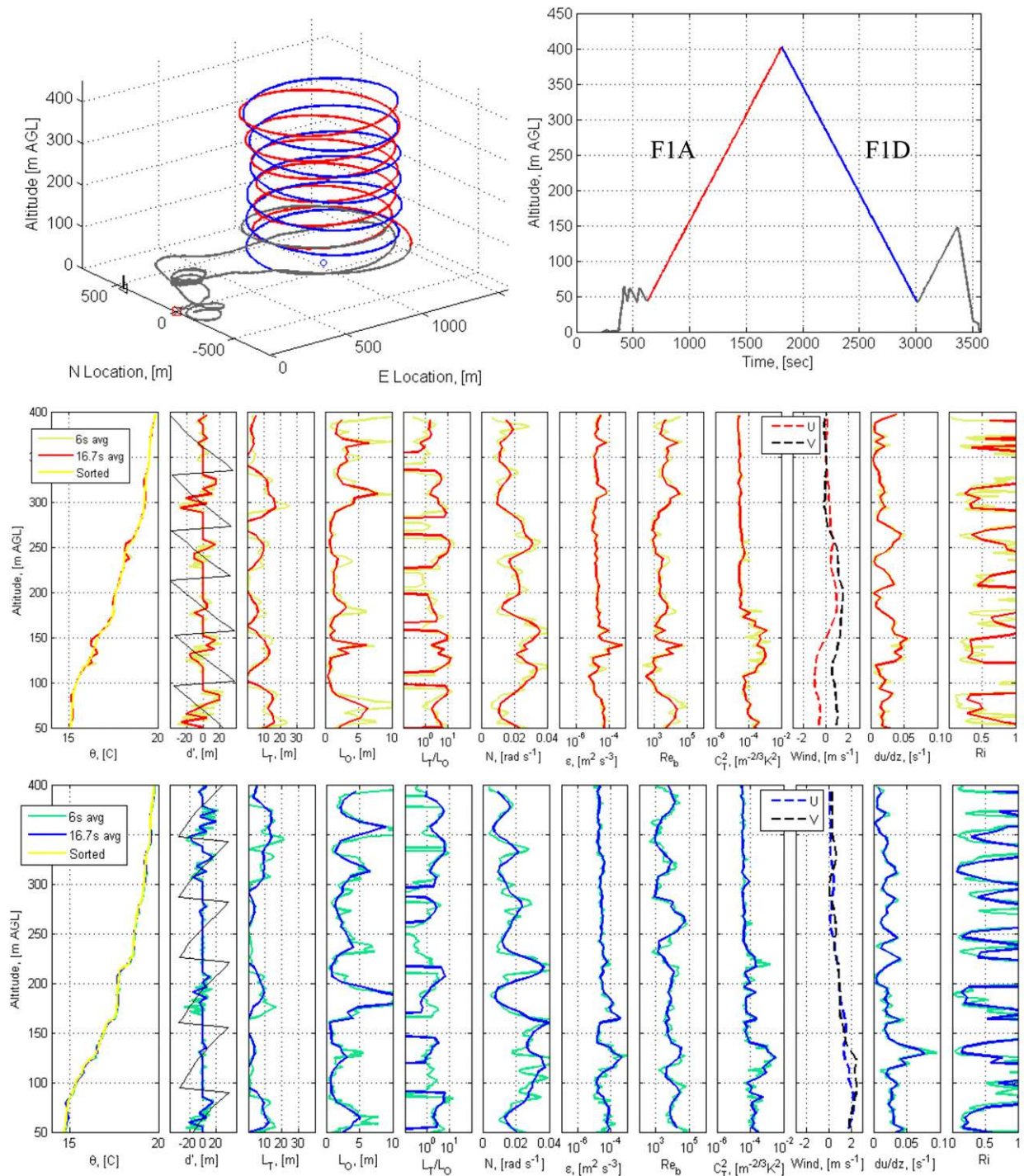The DataHawk flights occurred at ~1-h intervals and each included one ascending and one descending helical

FIG. 3. (top left) F1A and F1D circular flight paths, and (top right) altitude–time profile beginning at 0758:17 LT 11 Oct 2012. Profiles of θ, d', L_T, L_O, L_T/L_O, N, ε, Re_b, C_T^2, u and v, du_h/dz, and Ri for the (middle) ascending and (bottom) descending profile sets. See text for further details.

profile over 40 min from ~50 to 400 m above ground level (AGL) at the DPG East Slope site. The horizontal and vertical velocities were ~14 and 0.3 m s^{-1}, respectively. For the three flights, the circle diameters were ~900, 1500,

and 1200 m, respectively, and the helix depths were ~60, 100, and 80 m per circle, respectively. The spiraling flight paths and altitude–time plots for each flight are shown in the top panels of Figs. 3–5, respectively. Also
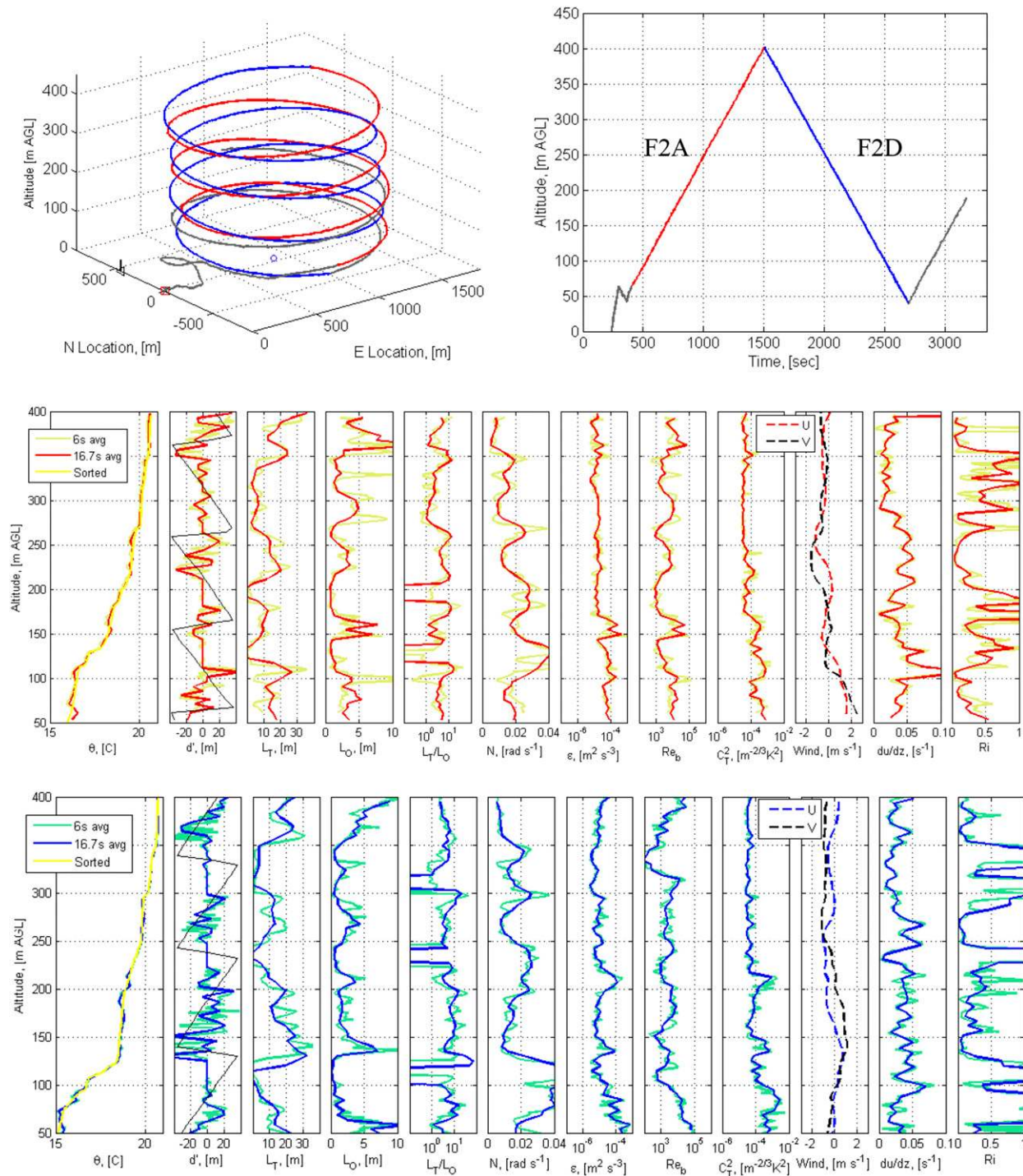
FIG. 4. As in Fig. 3, but for flight 2 beginning at 0902:27 LT 11 Oct 2012.

shown are measurements for each flight plotted against altitude [middle ascending (red), bottom descending (blue)] processed as described in the previous section at 1.8- and 5-m averaging resolution, except for winds, which have a 4.5-m vertical resolution. As discussed later, these vertical profiles should not be mistaken for vertically sampled flows. These profiles include the following column plots, in order:
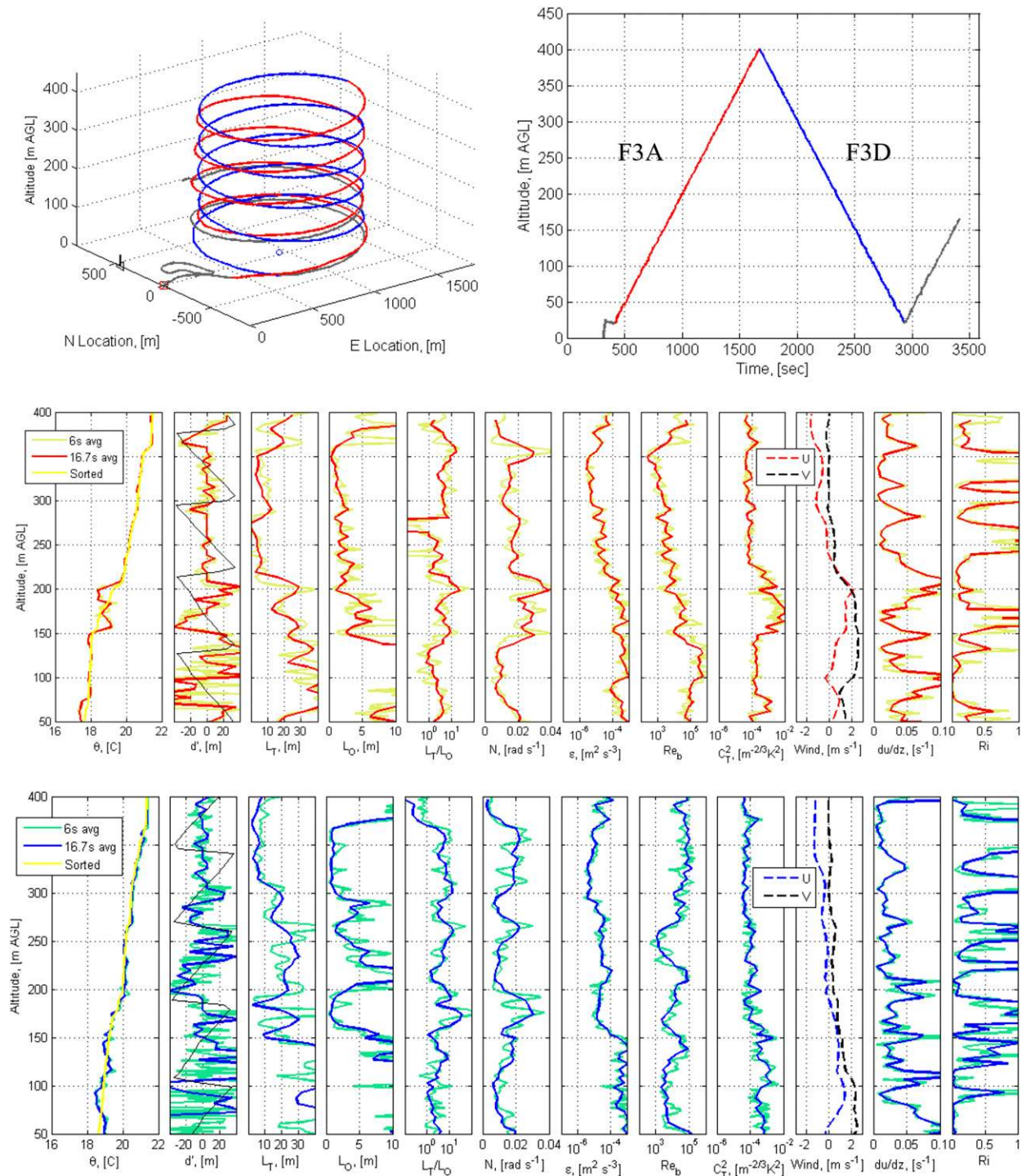
FIG. 5. As in Fig. 3, but for flight 3 beginning at 1004:28 LT 11 Oct 2012.

1) unsorted and "Thorpe sorted" potential temperature θ (°C)
2) Thorpe displacement d' (m)
3) Thorpe scale L_T (m)

4) Ozmidov scale L_O (m)
5) inverse of the ratio of Ozmidov to Thorpe scale $C^{-1} = L_T/L_O$, because L_T can be zero
6) buoyancy frequency N from Thorpe-ordered θ (rad s^{-1})

7) turbulent mechanical energy dissipation rate ε ($m^2\,s^{-3}$)
8) buoyancy Reynolds number Re_b
9) turbulent temperature structure parameter, C_T^2 ($K^2\,m^{-2/3}$)
10) wind components u and v ($m\,s^{-1}$)
11) vertical shear of horizontal wind du_h/dz (s^{-1})
12) local Richardson number Ri

Collectively, these profiles suggest a relatively dynamic environment spanning this ~3-h [~0800–1100 local time (LT)] interval. The stratification is seen to be larger, but quite variable, at lower altitudes (below ~200 m) during the first two flights, with more adiabatic conditions below ~150 m on the third flight, perhaps accompanying an evolving daytime convective boundary layer. Evidence of S&L structures in θ, and of apparently incipient, active, or decaying instability events, is seen throughout the three flights. The vertical scales of the S&L structures in θ (and N) coincide with variations of other parameters as well. The most consistent correlations occur between the layers in θ and other indications of local instabilities or their effects, particularly large L_T, L_O, ε, and sometimes C_T^2, and small Ri. Specific examples include the following:

1) The maxima of L_T and L_O are often correlated, but the magnitudes vary widely, and there are also cases where one is large and the other is very small (large and small $C^{-1} = L_T/L_O$).
2) The term N is most often anticorrelated with ε and the larger of L_T and L_O, suggesting that the consequences of local instabilities are most often seen in layers.
3) The terms ε and C_T^2 are often closely correlated, but there are examples where ε is large and C_T^2 is small where the atmosphere is nearly adiabatic.
4) Small Ri is frequently correlated with large L_T and/or L_O, suggesting initial instabilities or their consequences.

Referring to the θ and N profiles in Figs. 3–5, we note tendencies for both more distinct S&L features and smaller vertical scales on flights 1 and 2 and less distinct S&L features and larger vertical scales on flight 3, apart from the single, large, apparent overturning event seen in the ascending profile of flight 3 (denoted F3A, with similar notations for the other flights). There is also an apparent evolution of the initial flow from stronger instabilities on F1A to later-stage events and a restratifying flow below ~300 m. Decreases of d' and L_T and the significant reductions of $C^{-1} = L_T/L_O$ on F1D all suggest decaying instabilities at this time. The observed decreasing strength of S&L features and their increasing vertical scales are roughly consistent with the hypothesis of flow evolution from strong initial instabilities to decaying instabilities and turbulence (see the comparisons with the modeling results below). At later times, F3A and the decending profile of flight 3 (F3D) exhibit increasing θ at the lowest altitudes by ~2–3 K, likely accompanying an intruding convective lower boundary.

Two aspects of these data at early times raise questions, however. One is the large d' and L_T variations at small vertical spacings. The second is a virtual absence of $d' \neq 0$ at the southern extent of each circle on F1A, where the thin black bearing line in the d' plot snaps from negative to positive (scaled to $-180°$ to $+180°$). Thus, one might ask whether the observed variations on the slant path are primarily due to variations in the vertical or the horizontal. Note that DataHawk horizontal and vertical velocities of ~14 and $0.3\,m\,s^{-1}$ produce flight paths that change altitude only 1 m in ~45 m traveled horizontally. Vertical flow displacements at small horizontal scales could easily account for the large d' and L_T variations at small vertical spacings. Their occurrence preferentially in one part of the ~900-m-diameter circles could accompany horizontally localized dynamics extending over the lowest ~400 m.

The presence of a stationary horizontal structure is dispelled by subsequent measurements. Both the flight circles and S&L features increase in depth on successive flights, but the correlations noted above are no longer present, suggesting that the variations of the different quantities shown in Figs. 3–5 are due to layering in the vertical, rather than extended in the vertical over an isolated lateral region.

However, this does not dispel the concern that horizontal variations may be adversely affecting the vertical profiles, leading to the misquantification of particular parameters or to the misinterpretation of the underlying features of the flow. We address the potential for such errors in what follows, first by examining some parameter variations as a simultaneous function of vertical and horizontal vehicle motions for suspicious horizontal structure, and second by comparing vertical and slant-path sampling in similar anticipated dynamics described by high-resolution direct numerical simulation (DNS) in section 4 below.

b. DataHawk slant-path profiles

Figure 6 shows both horizontal and vertical vehicle motion by plotting the horizontal arc length on the flight trajectory helix versus altitude at 2-s intervals (black dots). Measured deviations of θ' and horizontal wind deviations (u', v') are superimposed onto the location data as vertical displacements from each corresponding
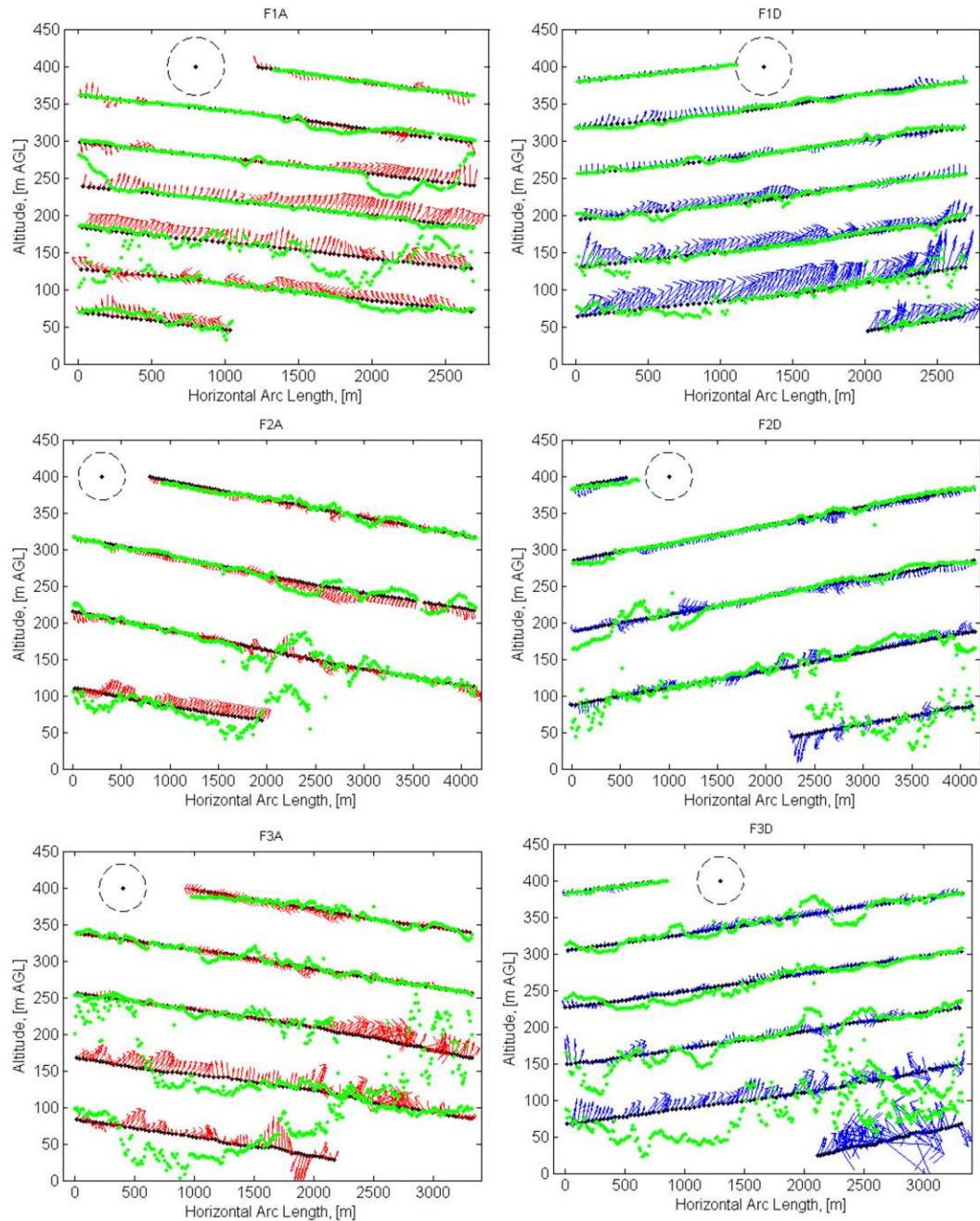
FIG. 6. Horizontal vs vertical DataHawk location (black dots) for the (left) ascending and (right) descending segments of (top to bottom) flights 1–3 on 11 Oct 2012. Wind velocity shown as vectors with components u' (to the right) and v' (up), with reference circle radii of $3\,\mathrm{m\,s^{-1}}$. The term θ' is shown (green dots) as a vertical deflection from the corresponding location, scaled in magnitude to make the variations visible.

black dot (for θ') and as vectors emanating from each black dot indicating u' (to the right) and v' (upward) components of wind at that location. Arc length is referenced to zero at the north bearing on the circle and is positive clockwise. Note that all flight paths are counterclockwise on the helix, producing negative-going arc

length with time. Shown are ascending and descending profiles (left and right) for the three DataHawk flights discussed above (from top to bottom).

The first ascending profile in Fig. 6, F1A, exhibits significant θ' and (u', v') extending from ~ 70 to $260\,\mathrm{m}$ altitude at along-track scales of $\sim 100\,\mathrm{m}$ and larger.

These are well correlated and large over several cycles at ~130–160 m, suggesting horizontal variations that account for the apparent vertical gradients seen in Fig. 3. The significant amplitudes and the anticorrelation between θ' and (u', v') suggest large-amplitude KHI in a wind shear having $du/dz > 0$ and $dv/dz > 0$, as is seen to be the case in Fig. 3 (see discussion of Fig. 12 below). These features also correlate with a locally enhanced ε and a broader C_T^2 enhancement at these altitudes. Additional large θ' and (u', v') are seen at ~230–260 m that account for the apparent overturning in Fig. 3, but the largely east–west sampling at this location makes a confident interpretation challenging.

The first descending profile, F1D, exhibits strong variability primarily in v' from ~100 to 230 m, small-scale and small-amplitude θ' at ~100 m, and large and chaotic θ' accompanying the strongest (u', v') at ~110–140 m. There is similarity in spatial scales between successive descending circles, but no obvious connection between these dynamics that would indicate a stationary horizontal structure. Continuing (u', v') occur in a previously mixed region at ~140–200 m having elevated ε. The more significant dynamics at ~100–140 m suggest vigorous overturning and mixing accompanying a large $dv/dz < 0$. These features and the significant ε and C_T^2 at these altitudes again suggest the late stages of local KHI.

Turning to F2A, we see small-scale features in θ' and (u', v') having apparent horizontal scales of ~30–150 m or greater at several altitudes. Large-scale and large-amplitude θ' in the nearly adiabatic layer below ~100 m may indicate true overturning, given that large ε and C_T^2 also occur at these altitudes. A layer at ~130–170 m exhibits significant θ' and v' at ~80-m along-track scales that correspond to significant apparent d' and enhanced ε and C_T^2. These occur in a region of significant mean shear and stability, suggestive of potential KHI at this altitude and time. Also of interest are the θ' at ~200–260 and ~330–370 m altitudes. These appear to be coherent between the upper two circles, to have ~150-m along-track scales, and to be correlated with winds toward the south-southwest at ~200–260 m. Such in-phase correlations of θ' and (u', v') also suggest possible KHI at ~250 m altitude having an alignment along the north-northeast–south-southwest plane with $dv/dz > 0$, as observed in Fig. 4.

Slant-path plots for F2D exhibit similar fluctuations at ~50–80 m, again because of a nearly adiabatic layer with potential overturning and large d'. An apparent quadrature relation between θ' and v' suggests local GW propagation below ~150 m where mean shears are weak. The term θ' and a small v' at higher altitudes may also signal decaying turbulence at ~180–300 m.

Slant-path plots for F3A suggest a convective boundary layer extending to ~150 m, with possible convective penetration to ~200 m. It is also possible, however, that the developing convection led instead to a strongly stratified and sheared interface that initiated strong KHI between ~150 and 200 m, given the correlated $\theta' < 0$ and $v' > 0$ near 150 m. The profiles of ε and C_T^2 confirm the inference of strong turbulence extending to above 200 m. F3D profiles are similar to F3A profiles in many respects, with fairly coherent and correlated θ' and north-northeast–south-southwest motions at an along-track scale of ~100–150 m at altitudes of ~70–130 m. Indeed, this coincides with local maxima of $du/dz < 0$ and $dv/dz < 0$ (consistent with a KHI interpretation), and of ε and C_T^2.

Overall, these data are consistent with the expected instability types and scales in stratified flow, suggesting that the slant-path sampling does not introduce *qualitative* artifacts when viewed as the vertical and slant-path profiles shown. This is encouraging; it implies that such measurements may be used to detect the presence of various forcing influences and to qualitatively assess stages of resulting turbulence evolution. This would be useful in a field campaign as a prospecting tool to identify the presence, location, and scale of flow features for possible further examination in more detail. Such data can also provide validation checks for high-resolution measurements, for example, examination of horizontal correlations between circles that could cause false indications of vertical structure.

On the other hand, it is difficult to assess the *quantitative* errors that may be introduced by this slant-path measurement and analysis process, because the underlying dynamics are not known. We now turn to a DNS of gravity wave–finescale (GW–FS) interactions exhibiting small-scale dynamics that appear to be similar to DPG measurements to help evaluate and interpret the DataHawk results described above through comparisons of DataHawk ''vertical'' and slant-path profiles with those from the DNS. A DNS designed specifically to approximate the DataHawk as closely as possible would of course be desired. But this would be very challenging without a far more complete specification of the larger-scale motions and thermal structure spanning the DataHawk measurements at larger spatial scales.

4. Multiscale DNS fields, and vertical and slant-path profiles

Initial DNS studies of multiscale flows driven by GW and oscillatory mean shear superpositions and an idealized DNS of KHI that compared very well with observations at higher altitudes were performed by Fritts et al. (2009, 2013, 2014). DNS results employed here were described by Fritts et al. (2014, 2016).

The multiscale DNS fields arise from a single initial GW having a potential temperature amplitude gradient of $d\theta'/dz = 0.5\, d\theta_0/dz$ and an intrinsic frequency of $N/10$—hence, a stable GW and a shallow propagation angle—and a superposed oscillatory mean shear having a ~5 times smaller vertical wavelength and a minimum initial Ri = 0.5 (see Fritts et al. 2016 for details). Despite the simple initial conditions, they nevertheless yield highly complex flows accompanying nonlinear interactions and instabilities. The KHI DNS assumed a KH wavelength of 100 m, Re = 2500, and an initial Ri = 0.10, leading to a maximum KH billow depth prior to a breakdown of ~50 m (see Fritts et al. 2014 for details). These are necessarily different in their details from the DataHawk observations because instability dynamics and turbulence intensities depend strongly on their local environments and forcing dynamics. Hence, specific comparisons will surely be somewhat speculative because small-scale instabilities can have a diversity of scales and forms. However, we expect the implications of individual instability events for profiles of the quantities shown in Figs. 3–5 to depend more on instability type and intensity than on the larger-scale environment. The multiscale and idealized KHI DNS likely yield representative instability and turbulence scales, intensities, and character. Indeed, many of the features seen in the DataHawk profiles (noted in parentheses below) were seen to compare reasonably with those observed in the DNS results. Examples include the following:

1) strongly stratified sheets with large positive $d\theta/dz$ varying in depth from a few meters to ~10 m or more (F1D, F2D, and F3A)
2) weakly stratified layers having small d', L_T, ε, du_h/dz, and Ri varying in depth up to ~50 m or more and suggesting previous mixing events or strong GW advection (all profiles)
3) nearly adiabatic layers having large d' and L_T, possibly larger ε, small du_h/dz and Ri, and varying in depth from ~20 to ~50 m or more, suggesting restratifying turbulence events (F1A at ~80 and 310 m; F1D at ~70 and 180 m; F2A at ~370 m; F3A at ~100–150 m)
4) apparent overturning having locally large negative $d\theta/dz$ with wind shear and/or small Ri, suggesting active KHI (F1A at ~150 m; F2A at ~100, 160, and 240 m)
5) sharp C_T^2 maxima at the edges of adiabatic or weakly stratified layers that are displaced relative to ε maxima (F1D at ~170 and 220 m; F2D at ~80 m; F3D at ~70 and 180 m)

Figures 7–9 show streamwise-vertical (streamwise) cross sections of the u, v, w, θ', ε, and N^2 fields from a GW–FS DNS at 10, 12, 14, and 16 buoyancy periods, T_b [see Fritts et al. (2016) for a more complete discussion of the DNS methodology]. The term θ' rather than θ, ε, and N^2 computed from reordered θ are shown in order to display the effects of advection, regions of instabilities and turbulence, and the S&L structures in θ contributing to, and arising from, these dynamics more clearly. As noted above, these fields arose for an initial GW–FS flow that was not guided by DPG measurements, but which appears to capture many aspects of the observed dynamics. The times displayed in Figs. 7–9 were selected to span a range of dynamics yielding similar S&L character. A model domain depth of 500 m (and a width of 1000 m) was chosen to yield comparable S&L scales and streamwise velocity variations of ~2–3 m s^{-1}.

a. GW–FS DNS cross sections

Figures 7–9 reveal significant layering in all fields except w. These features comprise the S&L structures that are maintained by GW–FS interactions throughout the evolution. Larger-scale, largely two-dimensional (2D), wave–wave interactions account for the quasi-horizontal S&L structures, their strong shears that drive local KHI, and the GW overturning and intrusion events observed at multiple times and locations. These initial ~2D instability events account for the larger-scale, and larger amplitude, coherent features seen in u, w, θ', ε, and N^2 throughout the interval shown. Examples include 1) active and incipient GW breaking at upper left and center right at 10 T_b, 2) KHI at upper right at 12 T_b, 3) residual 3D turbulence from KHI at upper left and from GW breaking at lower right at 14 T_b, and 4) an intrusion comprising a shallow jet moving rapidly to the left at lower left at 16 T_b. Note, in particular, that large and correlated u, w, and θ' are indicative of significant GW and/or KHI events; negative N^2 indicates local overturning features; and large ε typically follows GW overturning and mature KH billows.

All of the small-scale dynamics seen in Figs. 7–9 exhibit ratios of vertical to horizontal scales dramatically larger than the 1/45 slope of the DataHawk flight paths. As examples, the GW breaking events at 12 T_b have ratios of ~1/3–1/1, the large KH billows at 12 T_b have ratios of ~1/2, and the intrusion at 16 T_b has a ratio of ~1/3. Even the larger-scale S&L structures implied by the u and θ' fields exhibit slopes often exceeding ~1/10 to 1/5. Hence, horizontal variations of the dynamical fields surely contribute to the variations seen in the slant-path DataHawk measurements shown in Fig. 3–5. Intuition suggests that if the features of interest are at similar vertical/horizontal aspect ratios as the sampling path, then resulting "vertical" profiles would be representative of true vertical sampling through those features.
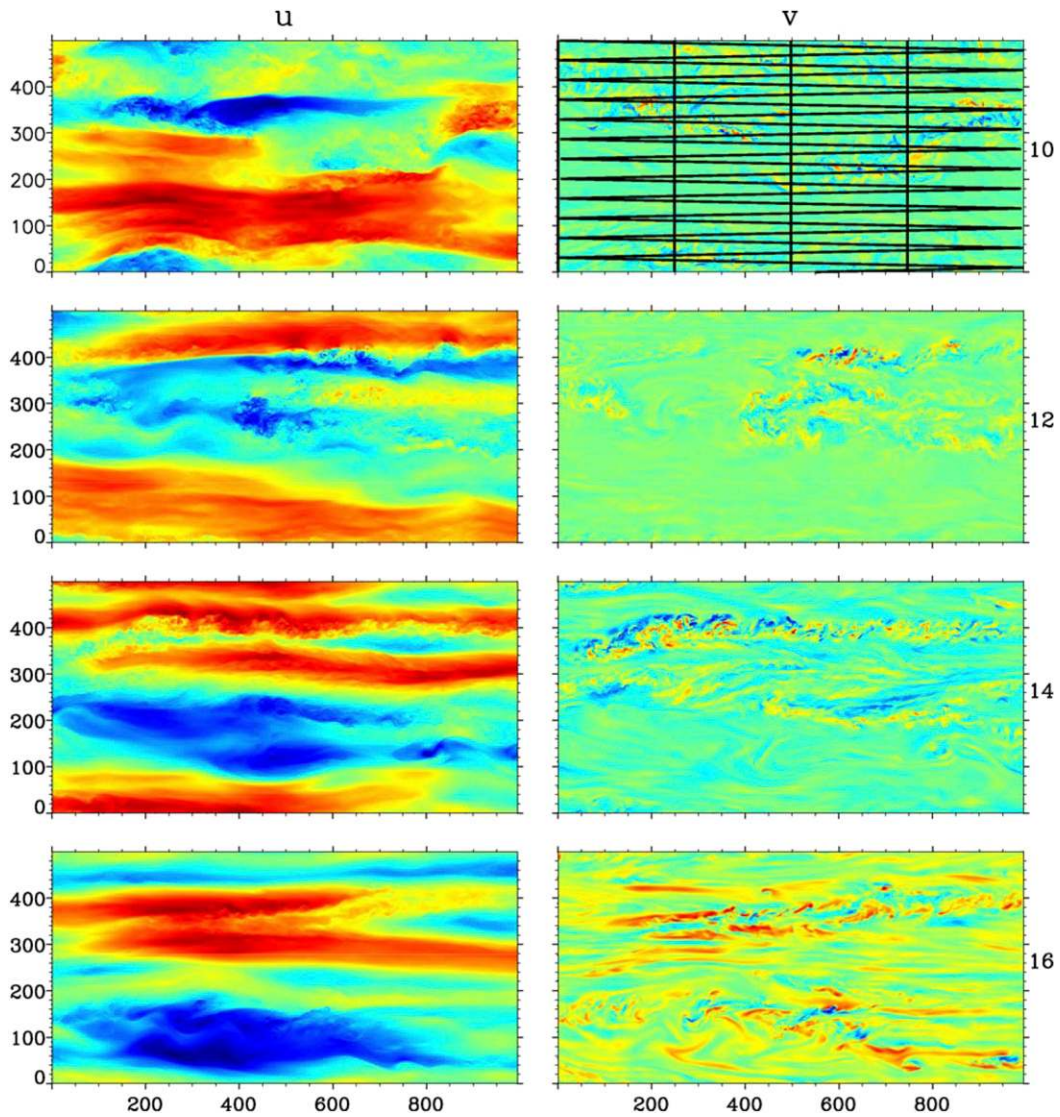
FIG. 7. Streamwise-vertical cross sections of streamwise and spanwise velocities, (left) u and (right) v, at times of (top to bottom) 10, 12, 14, and 16 T_b from the DNS described by Fritts et al. (2014). Note the significant layering structures in u throughout and in v at 16 T_b, and the coherent regions with nonzero v that arise accompanying the various instability and turbulence events that survive to late times. Colors show positive (red) and negative (blue) magnitudes with positive u to the left and positive v out of the page.

Likewise, variations in such measurements would be expected to be indicative of horizontal scales in those features, without undue influence from vertical variations. To assess the practical potential for biases in slant-path measurements, we examine the DNS results along alternative sampling paths for a direct comparison.

b. GW–FS DNS vertical versus slant-path profiles

We now compare streamwise cross sections of θ', u, and ε and infer d', L_T, and Ri along a 1:45 slant path (black) to four true vertical profiles spanning the streamwise domain at 0, 250, 500, and 750 m (shown with

red, and yellow, green, and blue lines, respectively) with the 6- and 16.7-s (1.8- and 5-m vertical) sampling employed for Fig. 6. Both results are displayed as vertical profiles at 10, 12, 14, and 16 T_b (top to bottom) for the 1.8- and 5-m vertical resolutions (left and right) in Fig. 10.

The left panels of Fig. 10 reveal both qualitative agreement and significant differences between the slant-path and vertical profiles. Clearly, we should not expect close agreement in altitude as a result of the horizontal variations seen in Figs. 7–9 at these times. Nevertheless, the slant-path θ profiles indicate an evolution from more
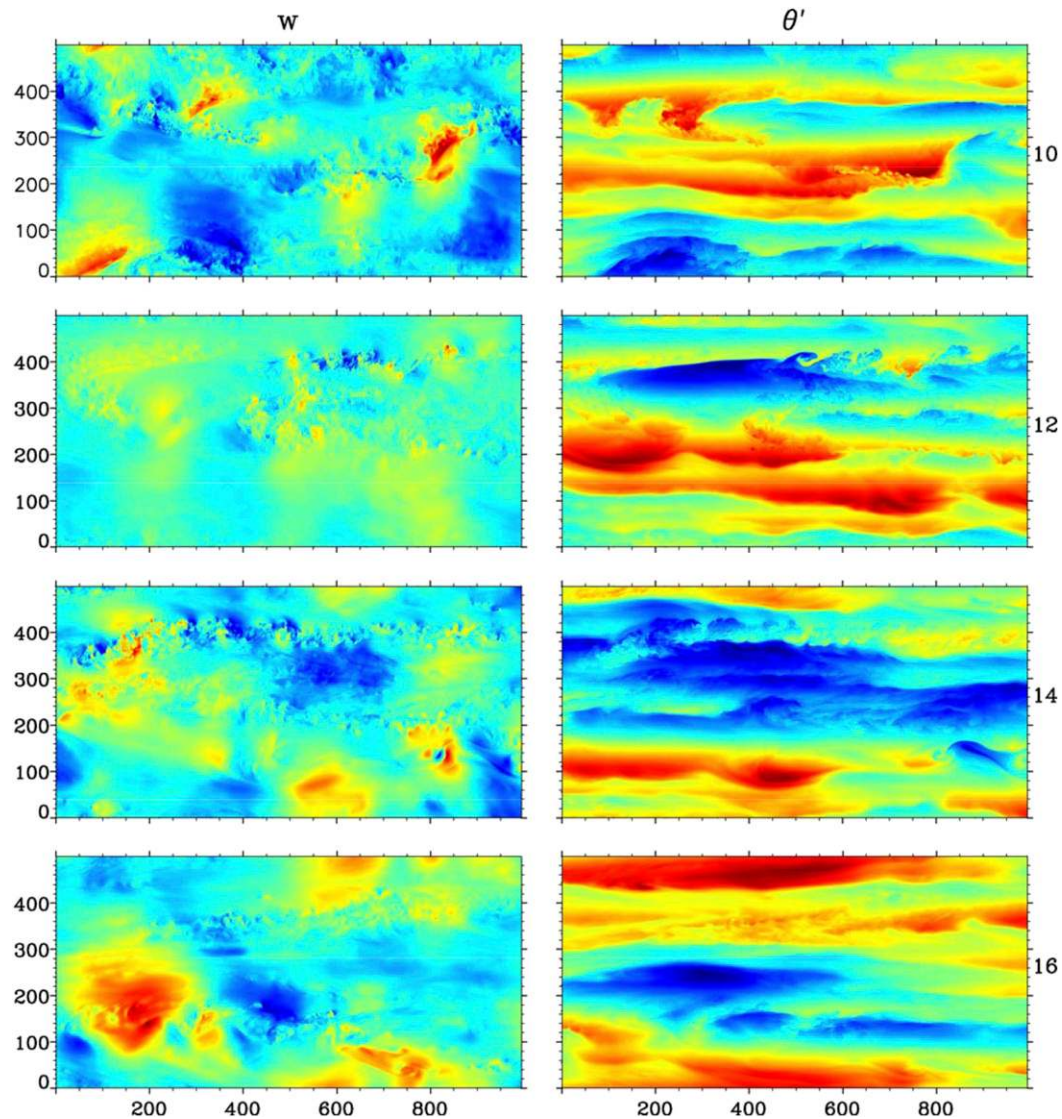
FIG. 8. As in Fig. 7, but for (left) w and (right) θ'. Note the strong layering in θ' that correlates closely with that seen in u. Maxima of w instead highlight regions of local GW and instability dynamics.

distinct to much weaker S&L structures over the 6 T_b displayed that agrees reasonably with those seen at each vertical profile location. Likewise, slant-path and vertical ε profiles suggest intermittent, larger magnitudes accompanying discrete events at 10–12 T_b and decreasing magnitudes, broader distributions, and closer agreement as turbulence magnitudes decrease and layers become more uniform. Slant-path and vertical profiles of u, and inferred d', L_T, and Ri exhibit significant differences at all times but are somewhat closer in agreement at larger vertical scales at 12 and 14 T_b. The slant-path profiles at 10 and 16 T_b exhibit generally larger fluctuations at larger apparent vertical scales accompanying horizontal GW variations initiating

instabilities at ~10 T_b and persisting to late times as instabilities and turbulence subside.

Major differences in the profiles of d', L_T, and Ri arise between the vertical and slant-path sampling at smaller vertical scales. These slant-path features have no counterparts in the true vertical profiles and obviously arise from horizontal gradients in these quantities that do not have significant vertical gradients at corresponding vertical scales; that is, the feature aspect ratio is significantly different than the sampling path. Large negative $d\theta/dz$ and large du/dz at small vertical scales in the slant-path profiles are often ~10 times larger those seen in the true vertical profiles. Large negative $d\theta/dz$ yield large inferred d' and L_T where real values are often
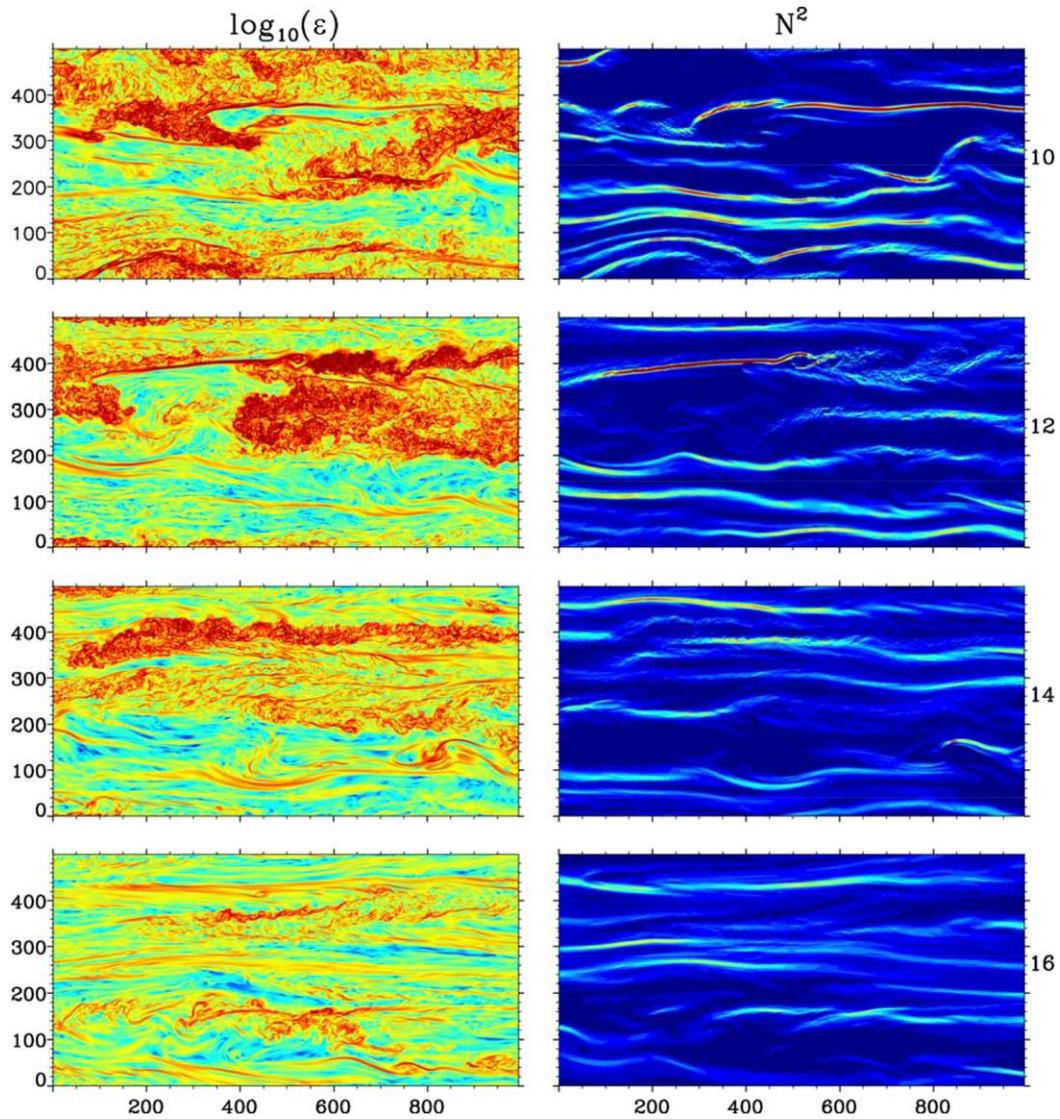
FIG. 9. As in Fig. 7, but for (left) ε and (right) N^2 computed from reordered θ. Note the strong layering in θ' that correlates closely with that seen in u. Strong layering is seen in both fields. The strongest turbulence is seen to occur in weakly stratified regions as a result of strong mixing. Colors in the fields indicate values from zero (dark blue) to strong maxima (red).

small or zero. Large du/dz and negative $d\theta/dz$ at small vertical scales likewise yield small and/or negative Ri where real values are large and positive. The differences in these profiles suggest caution in interpreting shallow slant-path measurements as high-resolution vertical profiles in cases where small-scale GW and instability dynamics have large influences. Where slant-path sampling occurs in more quiescent regions exhibiting more nearly horizontal S&L structures, or where shallow S&L slopes are opposite of the sampling path (inducing a larger path slope relative to the flow), slant-path measurements more closely approximate true vertical profiles.

Given the above findings, one might expect that coarser vertical resolution for slant-path and vertical profiles to yield closer agreement by removing influences of small-scale, but significant, horizontal gradients. Indeed, the right panels of Fig. 10 reveal that larger vertical averaging can remove biases accompanying implied small-scale vertical variations and improve agreement between profiles in some cases. See, as examples, the θ and u at 12 and 14 T_b. Also, estimates of ε are not significantly impacted by slant-path sampling, apart from the potential to suggest smaller-scale variations in the vertical than in reality where significant horizontal gradients occur.
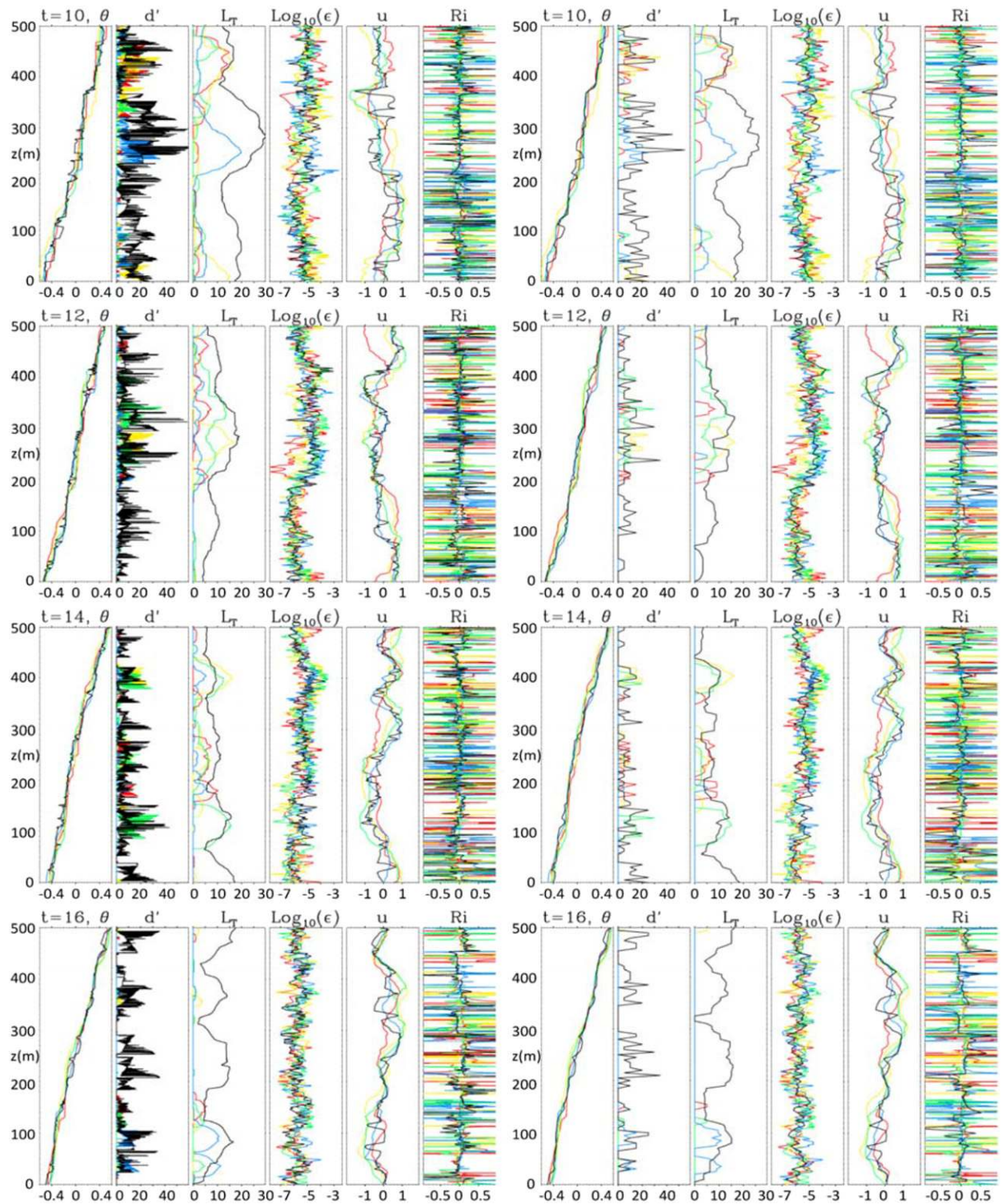
FIG. 10. Vertical and slant-path profiles of nondimensional θ, d', L_T, log e, u, and Ri at (top to bottom) 10, 12, 14, and 16 T_b from the cross sections shown in Figs. 7–9 for comparison with those measured by the DataHawk. Vertical profiles at horizontal locations of 0, 250, 500, and 750 m are shown with red, yellow, green, and blue lines, respectively. Black profiles are obtained along the black paths shown at upper right in Fig. 7. Profiles obtained with (left) 1- and (right) 6-m vertical resolutions.

Estimates of d' and L_T derived from $d\theta/dz$ also appear to be reasonable (but somewhat enhanced) where slant-path sampling coincides with true vertical overturnings and in relatively adiabatic regions having significant horizontal extents. However, large biases occur where large inferred negative $d\theta/dz$ and large d' arise from horizontal rather than vertical gradients accompanying strong GWs and instabilities at 10 T_b, and at 16 T_b as instabilities and ε subside, but horizontal variations at larger scales remain. See, as examples, the profiles below 200 m at 10 and 12 T_b and those above ~200 m at 16 T_b. An even larger vertical smoothing would further enhance the agreement, but at the expense of less sensitivity to the smaller scales of interest.

Large fluctuations of Ri occur in both vertical and slant-path profiles at both resolutions. For the vertical profiles, these are due to true small-scale θ' (with often nonzero d') and du/dz. In these cases, occurrences of negative and small positive Ri are correlated to some degree with larger L_T and ε. For the slant-path profile, additional apparent small-scale θ' and du/dz arise as a result of horizontal variations in these quantities and can lead to large errors in Ri estimates.

Despite the potential for exaggeration of small-scale d' and L_T where true values may be small or absent, and similar elevated estimates of du/dz and dv/dz, yielding smaller Ri than what occurs in reality, slant-paths are required by fixed-wing aircraft and these measurements provide a rich set of information, if properly interpreted. This is investigated below by employing DNS studies of ''known'' features sampled in this way, to better understand what information can be extracted from such measurements.

c. DNS slant-path ''measurements''

To further aid our understanding of the slant-path DataHawk profiles shown in Fig. 6, we show similar slant-path sampling of θ' and (u', v') from the GW–FS DNS at 10, 12, 14, and 16 T_b in Figs. 11 and 12, with θ' shown in green as vertical displacements and (u', v') shown as red vectors clockwise from the direction of primary GW propagation. Here, sampling is confined to the streamwise plane, with path reversals at the domain edges in order to maintain continuous fields and dynamical influences. For the assumed DNS depth of 500 m, each slant-path segment extends 1 km horizontally. Thus, each segment corresponds to aproximately one-quarter to one-third of the circumference of the DataHawk flight circle from DPG in each case, and the sampling resolution is at 14 m along track and 1 m in the vertical, for comparison with the DataHawk measurements.

Referring to the sampling at 10 T_b (at top in Fig. 11), we see several layers of enhanced small-scale activity.

At upper left (second and third profiles from top) θ' and u' are approximately anticorrelated accompanying local GW breaking (see the upper panels in Figs. 7–9). At middle left (fourth and fifth profiles from top) and far right (fifth and sixth profiles from top), θ' exhibits horizontal gradients with weak u' corresponding to a previous GW breaking event. At lower right (bottom two profiles) θ' exhibits significant perturbations, but u' perturbations are weaker, as a residual of a previous KHI event having $du/dz < 0$.

Turning to the DNS sampling at 12 T_b in the middle panel of Fig. 11, we see coherent perturbations in θ' and u' that exhibit significant correlations at several sites. At upper center and right (top two profiles), we see oscillatory θ' and u' that are well correlated where KH billows are forming (center, also see the second panels of Figs. 7–9). Where strong mixing has already occurred in the KH billow, however, we see large u' but smaller θ' (upper right; also see the KHI profiles at the final time after significant billow core mixing in the lower panel of Fig. 12). Finally, seen at lower center and left (second profile from bottom) are anticorrelated θ' and u', indicating initial stages of KHI where $du/dz > 0$.

DNS slant-path profiles at 14 T_b (Fig. 11, lower panel) exhibit significant θ' and u' perturbations throughout the domain that are residuals of KHI and strong mixing at the edges of several previous fluid intrusions. These vary from correlated to anticorrelated, depending on the sign of du/dz. The terms θ' and u' are typically correlated (anticorrelated) at the upper (lower) edges of local u maxima having $du/dz < 0$ (>0). The one clear GW breaking event seen at lower right in the θ' and w' cross sections in Fig. 8 (see the large $w' > 0$ where $\theta' < 0$), with $w' < 0$ and $\theta' > 0$ to the left (upstream) occurred between the second and third profiles from the bottom and were not sampled.

The DNS slant-path profiles at 16 T_b (Fig. 12, upper panel) likewise reveal θ' and u' perturbations that exhibit significant correlations. The streamwise scales of these perturbations are typically larger than seen at earlier times, now varying from ~100 to 300 m for the streamwise domain of 1 km. As at 14 T_b, θ' and u' are largely correlated or anticorrelated, with the perturbations arising largely at the edges of earlier intrusions. As examples, see the lowest three profiles at center and right. However, local GW breaking also occurs at this time at lower left and accounts for the quadrature among θ' and u' seen at the center and left in the second and third profiles from the bottom at this time (also see the strong θ' and u' perturbations at lower left in the lower panels of Figs. 7 and 8). The lower panels of Fig. 12 show spiral sampling at 14 m s^{-1} relative motion of a series of KH billows at three stages of the evolution
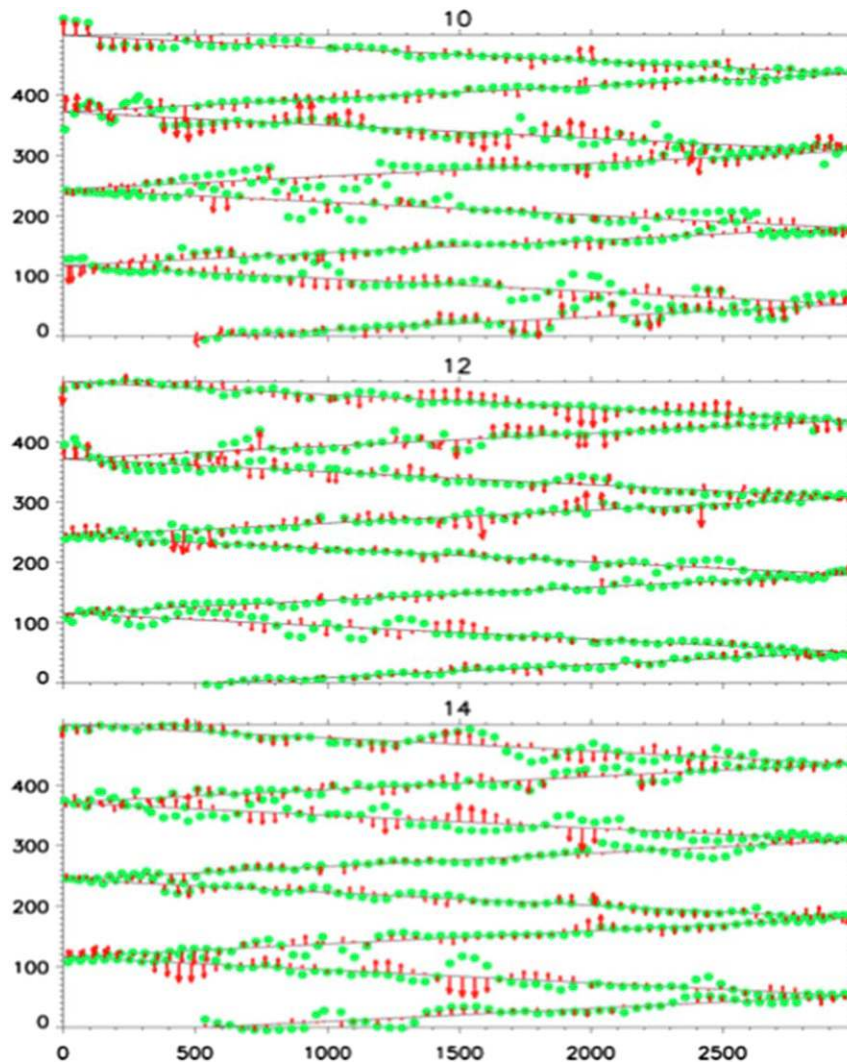
FIG. 11. As in Fig. 6, but for nondimensional (u', v') and θ' along slant paths in the streamwise-vertical DNS planes shown in Figs. 8 and 9 at (top to bottom) 10, 12, and 14 T_b. As seen in the DataHawk measurements, there are frequent correlations between u' and θ' that are indicative of specific small-scale dynamics and which induce spurious large apparent vertical gradients when displayed as vertical profiles.

with a circle diameter of 1 km and KH billow depths of ~50 m shown as vertical and slant-path profiles. At the initial time ($0\ T_b$), the larger u' and θ' near path angles of 0° and 180° exhibit strong coherence, that is, correlated (in phase) near the billow or shear layer centerline and anticorrelated (antiphase) in the lower billow edge region. At the upper billow displacement, however, the sampling has exited the billow and u' and θ' are very small. The correlations just described are still apparent at the intermediate time ($1\ T_b$) but are weaker in the lower edge region and at smaller scales near the billow centerline, because 3D instabilities have eroded the larger initial perturbations. At the final time ($2\ T_b$), the billow core and edge regions have become largely

turbulent and the θ profile has become nearly uniform in the plane of KH evolution, but there is a residual coherent billow in the u' field.

The simulated KHI sampling profiles suggest that identifying these dynamics based on correlations among u' and θ' is complicated, but they provide several options. Finescale fluctuations occurring within the billows exhibit clear, but transient and spatially localized, correlations at small spatial scales. Importantly, these correlations are fairly unique, as GW u' and θ' are normally in quadrature, except for ducted motions, which are unlikely to occur at very small spatial scales. Slant-path sampling without spiraling offers the potential to identify such small-scale fluctuations exhibiting
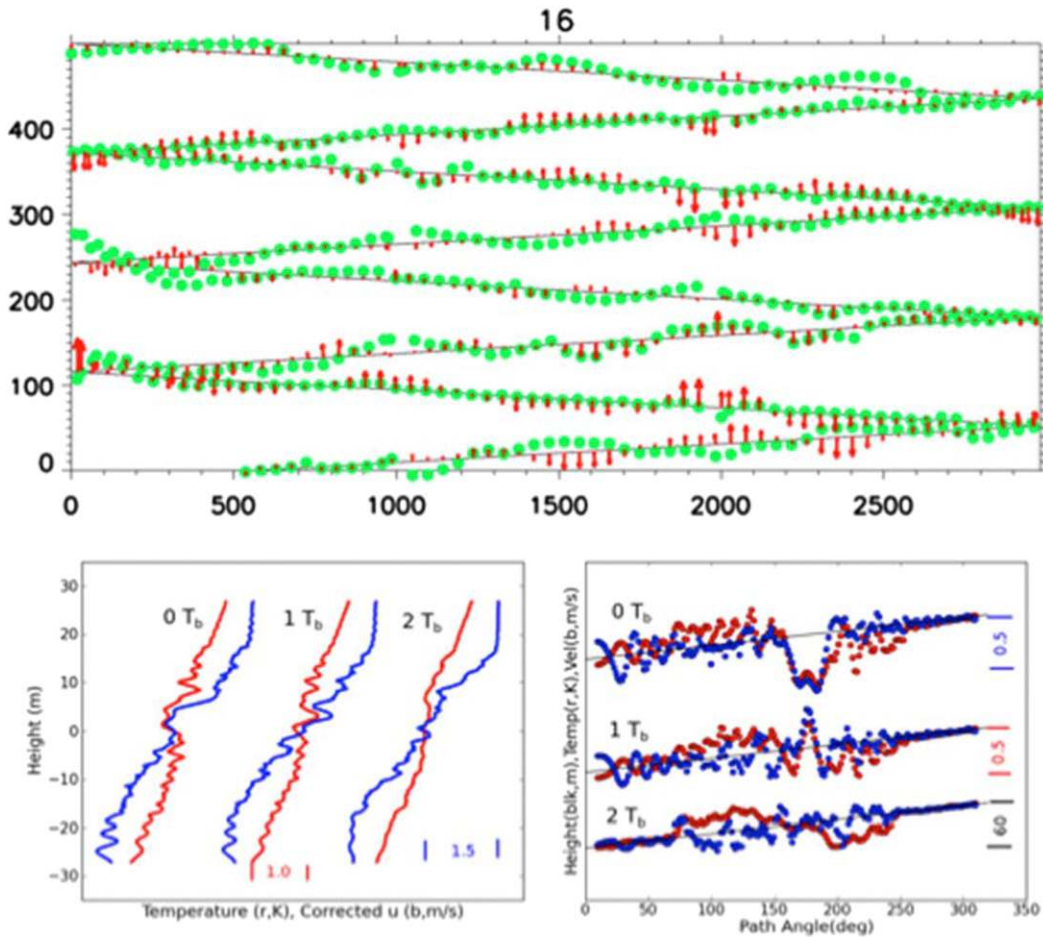
FIG. 12. (top) As in Fig. 11 (top) for 16 T_b. (bottom left) Vertical and (bottom right) slant-path sampling of u' (red) and θ' (blue) through a series of KH billows at three stages of their evolution (left to right in the left panel, top to bottom in the right panel) following maximum billow amplitude at 1 T_b intervals.

the horizontal periodicity of the KHI billows when sampling is along, rather than across, the plane of large-scale KHI motions. Such observations would be even more compelling in the presence of significant vertical wind shear and small Ri.

5. Discussion

We have performed high-resolution in situ measurements with a new DataHawk UAS along spiraling flight tracks that have revealed persistent, but evolving, S&L structures at altitudes from 50 to 400 m in the stable lower troposphere. We have also employed results from two high-resolution DNS—one of multiscale dynamics that describes the formation and evolution of similar S&L structures (Fritts et al. 2016) and a second of idealized KHI that agrees well with observations at higher altitudes (e.g., Fritts et al. 2014; Hecht et al. 2014—to aid in the assessment of the DataHawk measurement

capabilities and qualitative interpretations of the observed dynamics. A DNS specifically addressing the measured environmental conditions was not possible because of the present inability to adequately define the needed DNS initial conditions. Nevertheless, comparisons of the measurements and the DNS results revealed some significant similarities, cautions for DataHawk sampling strategies, and an ability to infer specific small-scale dynamics events based on correlations among the measured quantities.

Comparing DNS vertical and slant-path profiles reveals that significant biases can arise when slant-path perturbations are due to horizontal rather than vertical variations. Such biases can yield large inferred d' and L_T where true values may be small or absent. Similar biases can also elevate estimates of du/dz and dv/dz, yielding smaller Ri than what occurs in reality.

DNS slant-path profiles of θ' and u' reveal that correlations among these fields are relatively good indicators of specific small-scale dynamics occurring in

multiscale flows, especially KHI and GWs at early stages of their evolutions. This is because these fields exhibit coherent perturbations that are largely in-phase or antiphase for KHI and more nearly in quadrature for GWs. KHI is perhaps the easiest to identify, as these signatures can be seen at early stages and small amplitudes, throughout KH billow rollup, and even at late stages when the billows are turbulent but still coherent. Several events also reveal that coherent u' can persist but that θ' disappear, where KH billow turbulence and mixing yields nearly adiabatic layers. Such regions exhibit elevated ε that are indicative of an advanced stage of instability and turbulence evolution.

Vertically propagating GWs are likewise easy to identify where they exhibit nearly linear behavior, for which θ' and u' are expected to be in quadrature. This also appears to be the case at early stages of overturning (and regions of coherent negative N^2). However, GW breaking yields strong plunging and complex 3D vortex dynamics that quickly lead to turbulence and large local ε. For larger-scale events having larger Re, turbulence is strong (with large ε) and rapidly mixes over significant depths. It is possible to identify the consequences of these dynamics with reference to the DNS fields. However, the correlations between θ' and u' that accompany these later-stage GW dynamics are no longer simple to infer, and local large ε is a better indicator of event character at this stage.

In contrast, ducted (or vertically evanescent) GWs that can often occur would exhibit in-phase or antiphase correlations between θ' and u' that more closely resemble those caused by KHI. Large-scale ducted GWs spanning the volume have much larger horizontal and vertical scales than KHI, and most often relatively small slopes and vertical displacements. However, large events, such as solitary waves, can also occur, but exhibit distinctly different structures than KHI. Smaller-scale ducted GWs are also possible, in principle, given the highly structured environment in u and N^2, but these have yet to be detected in observations or in our DNS to date.

A number of intrusions were identified in our multiscale DNS, but they are challenging to identify in the slant-path DNS sampling using correlations of θ' and u', for which there is no specific expected relationship. However, our observations indicate that intrusions comprise local jets in the direction of primary large-scale GW propagation that frequently become turbulent at their upper and lower edges as they develop. This suggests that they should be identifiable as correlations of significant local u' and ε maxima along vertical or slant-path profiles intersecting them at some reasonable incident angle.

The results presented show that the ability to identify and quantify local instability and turbulence events in multisale flows will usually strongly depend on the sampling strategy and the quantities being measured. Strictly horizontal (vertical) in situ sampling yields good estimates of horizontal (vertical) scales and amplitudes, but both vertical and horizontal sampling cannot occur simultaneously on a single vehicle.

In cases where events are locally isotropic, such as turbulence patches arising from GW breaking, KHI, and intrusions, sampling in any direction yields equivalent information on local structure constants, dissipation rates, etc. The scales of these features in the vertical and horizontal can only be determined, however, by paths that have excursions in the vertical and horizontal, respectively, suggesting the use of slant paths that have components of both. Other events, such as GWs and KHI *prior* to turbulence generation, which exhibit phase propagation, significant coherent velocities, and/or horizontal and vertical wind shears, will yield biased estimates of local gradients with any sampling trajectory, since the measurements will always be observing directional derivatives that are unlikely to align with the local gradient. Despite this local inaccuracy, the structure of variations along a segment of the sampling path can provide useful information on locations and scales of events, at least in cases where phase speeds or differential velocities are *not* a significant fraction of the in situ sampling velocity. More quantitative knowledge of these motions can be obtained only by simultaneous or closely successive sampling along independent trajectories through the volume of interest. Otherwise, horizontal variations can be readily misinterpreted as variations in the vertical, and vice versa. As examples, horizontal variations in the motions fields or vertical displacements as a result of GWs or KHI sampled nearly horizontally (on shallow slant paths) may lead to the following misinterpretations:

1) apparent large and oscillatory θ' at small vertical scales and significant implied d' and L_T and negative Ri where true vertical profiles may have $d\theta/dz > 0$
2) similar horizontal variations of u' and/or v', suggesting large and variable du'/dz and/or dv'/dz at small vertical scales and much smaller Ri > 0 where the true Ri is large
3) apparent layering of properly measured quantities, such as ε and C_T^2, at much smaller vertical scales than what occurs in reality

Independent-direction sampling will therefore be needed to avoid these quantitative biases. A simultaneous approach would require at least two vehicles

traversing a given domain in linearly independent velocity vector directions. For helical slant paths, this could take the form of opposite-direction trajectories, ascending or descending in unison, but traveling in opposite arc-length directions. If the helix diameter is on the order of the horizontal scale size of features, this provides linearly independent samples of the directional derivatives, from which the true gradient vectors (averaged over the horizontal diameter) can be extracted. Higher spatial resolution could be obtained by two vehicles traveling the helix in the same direction, in order to remain in close proximity, but with vertically oscillating trajectories that are opposite in phase. Here, the period of oscillation could be significantly shorter than a circle diameter, providing simultaneous measurements averaged over much smaller volumes. This latter approach also suggests a single-vehicle strategy that provides independent measurements in close proximity: the vehicle would follow an oscillating vertical trajectory, and successive ascending and descending segment pairs form a set of independent measurements for gradient extraction over the whole period of the oscillation. This could be carried out on circular helix trajectories, or on straight slant paths, for example, aligned with the advection direction as recommended by DNS studies.

Finally, inspection of the DPG and DNS ε profiles reveals very good agreement in the range of magnitudes of ε throughout each multiscale evolution and the correlations of ε with apparent active and/or turbulent regions in the corresponding θ, L_T, ε, and Ri fields. Specifically, observed ε range from a typical background value of $\sim 10^{-5}\,\mathrm{m^2\,s^{-3}}$ to local maxima from $\sim 10^{-4}$ to $10^{-3}\,\mathrm{m^2\,s^{-3}}$, with ε decreasing with time, apart from the apparent strong instability event seen at ~ 150–200 m and the convective boundary layer below ~ 150 m on F3A. Similarly, DNS values exhibit typical means of $\sim 10^{-6}$ to $10^{-5}\,\mathrm{m^2\,s^{-3}}$ and similar local maxima from $\sim 10^{-4}$ to $10^{-3}\,\mathrm{m^2\,s^{-3}}$, with the larger maxima occurring at earlier times. In each case, the decreases of ε maxima with time coincide with the apparent weakening of the S&L features. Given the more confident measurements of ε (relative to estimates of quantities potentially biased by horizontal gradients), we regard these results, the S&L structures seen in θ, and the correlations between θ' and (u', v') that suggest specific small-scale dynamics as the most compelling evidence for our interpretation of the DPG measurements as typical multiscale dynamics.

Comparing our DataHawk measurement capabilities with measurements during the very well instrumented CASES-99 boundary layer experiment, we draw the following conclusions:

1) Both DataHawk and tethered profiling systems (e.g., Balsley et al. 2003, 2006) can define quasi-vertical profiles of atmospheric parameters at resolution much higher than ground-based sounders or instrumented towers, but they exhibit biases as a result of advecting (or propagating) horizontal gradients that depend on the slopes of the effective slant paths.
2) Horizontal DataHawk measurements are comparable to tower measurements at specific altitudes (e.g., Sun et al. 2002, 2004), but they can extend to much higher altitudes, and at flight versus advection velocities.
3) DataHawk measurements can replicate, with much higher spatial resolution, aircraft measurements (e.g., Fritts et al. 2003b) but with smaller spatial extent and larger biases in measurements of propagating structures (e.g., gravity waves and intrusions).
4) Multiple DataHawks can, in principle, significantly expand on previous measurements by simultaneous horizontal sampling at adjacent horizontal and/or vertical positions.

Our analysis and discussion above have identified both benefits and liabilities to DataHawk spiraling slant-path sampling of multiscale dynamics in the lower atmosphere. DataHawk flight and measurement capabilities are new and versatile. But measurements by one DataHawk are only possible along a specific flight profile, and any one profile cannot describe the structure or evolution of dynamics that evolve in 3D and time. Specifically, slant-path profiles lead to misrepresentation of specific parameters, especially $d\theta/dz$, d', L_T, and Ri, at small spatial scales. Similarly, spiraling profiles can bias, or fail to describe, spatial scales of events comparable to, or larger than, the spiral flight circle. Because DataHawk measurements simultaneously define $T\,(\theta)$, u, and v (and other derived quantities), however, they do provide the ability to recognize coherent motions at larger scales that provide valuable clues to the underlying dynamics driving turbulence events at smaller scales.

Importantly for future measurements, demonstrated DataHawk flight and measurement capabilities, their low cost, and the tested ability to fly multiple Data-Hawks simultaneously along different flight paths offer many possibilities for expanded, diverse, and more comprehensive measurement programs. Here, we describe three such options:

1) *Well-instrumented lower-atmosphere sampling programs, for example, as in CASES-99 or VTMX.* Extensive ground-based (towers, lidars, radars, and/or sodars), balloons and/or tethered in situ, and/or research aircraft measurements could benefit significantly by DataHawk measurements along multiple, repeated fight paths defining the evolving horizontal

and vertical structures of the atmosphere at scales not captured by coarsely spaced ground-based measurements. DataHawk measurements in such applications would likely focus on horizontal, and some slant-path sampling (to capture event vertical scales), in order to 1) link the measurements by other instruments at larger scales and 2) define the spatial and temporal scales of the smaller-scale dynamics accounting for atmospheric fluxes and evolution.

2) *Measurements extending to several kilometers accessible only by profiling instruments.* Such measurement programs could include ground-based lidars, radars, and/or sodars, in situ balloons and/or tethered systems, and perhaps research aircraft, but at high costs. As above, DataHawk measurements would be able to define the links between ground-based data obtained at larger horizontal spacings along multiple, repeated horizontal profiles. Repeated horizontal and slant-path profiles in the same, parallel, or orthogonal planes would characterize atmospheric dynamics, mixing events, and evolution at horizontal and vertical scales not captured by other instruments, and at a low cost.

3) *Measurement programs employing DataHawks and limited ground-based instruments.* Field programs employing primarily DataHawk measurement capabilities, supplemented by vertical profiling intended to define the structure and evolution of the larger-scale environment, are also envisioned. In such cases, limited balloon, profiling tethered sensor, and/or radar measurements would define the evolution of the environment on coarser spatial and temporal scales. Multiple DataHawks would sample smaller or larger domains (e.g., hundreds of meters to several kilometers horizontally and/or vertically) with multiple, repeated horizontal and/or slant-path profiling, depending on the scales of the dynamics suggested by the ground-based measurements. DataHawk slant-path profiling would also reveal smaller-scale dynamics not captured by ground-based sampling and enable a focus on such embedded instability and turbulence dynamics where these appeared to be of primary interest. Such programs would be at least 10 times smaller in cost than the field programs envisioned in options 1 and 2 above.

6. Conclusions

New DataHawk sensor and flight control technologies enable in situ measurements of atmospheric parameters of unprecedented versatility. The sensors enable direct high-resolution measurements or derived estimates of multiple parameters, among them T and θ, buoyancy frequency N, Thorpe scale L_T, Ozmidov scale L_O, mechanical energy dissipation rate ε, buoyancy Reynolds number Re_b, thermal structure parameter C_T^2, wind components u and v, and the local Richardson number Ri. DataHawk flight controls enable multiple types of flight paths, producing various sampling strategies. Results in this paper show that care is needed in selecting these strategies if significant biases are to be avoided. As such understanding improves, we expect these capabilities to contribute to significantly improved measurements in the future.

APPENDIX

Wind Estimation Error

Horizontal wind is estimated here as the vector solution to a geometric problem relating measured relative wind magnitude (scalar airspeed) and measured GPS velocities (vector ground speed) at two points on a path where the GPS velocity changes direction or magnitude. This is described in detail in Lawrence and Balsley (2013b). In particular, vehicle attitude is not utilized. The errors associated with this estimate are discussed in detail below. First, we discuss the errors caused by relative wind magnitude.

The relative wind vector magnitude is measured by pitot-static differential pressure, aligned with the longitudinal axis of the body. Relative wind direction is not measured, but the vehicle weathervanes into the relative wind with a well-damped time constant of about 1 s; that is, it follows the relative wind field directional variations (causing unmeasured side-slip and angle-of-attack errors) with an accuracy that improves with scale size, for example, from about 30% at 14-m scale to 4% at 50-m scale. Since the wind estimation algorithm averages pitot data over distances of 50 m, these smaller-scale weathervaning errors cause relative wind angular errors on the order of 4%. These have a cosine of the angle effect on the measured relative wind magnitude. For example, for a 50-m scale variation in transverse velocity of $5 \, \mathrm{m \, s^{-1}}$ (maximum angle variation of 20° at $14 \, \mathrm{m \, s^{-1}}$

nominal airspeed), the residual weathervaning error is 0.8°, resulting in a negligible velocity magnitude error. However, the angle of attack can also be varied by action of the elevator control. Wind tunnel testing of the DataHawk has measured errors of up to 0.8% in pitot relative wind magnitude per degree of angle-of-attack variation. Consider a sudden 5 m s^{-1} loss of airspeed, due to extreme wind shear. The resulting loss of lift would cause the vehicle to descend, and the vertical rate loop would increase the angle of attack by 3° to maintain climb rate, resulting in an airspeed measurement error of -0.34 m s^{-1}. The resulting pitch change would also be misinterpreted as a change in the direction of the relative wind, producing an error in the horizontal component of relative wind (about the nominal pitch angle of 7.5°) of -0.11 m s^{-1}. At the same time, the airspeed loop reacts with a decrease in elevation, causing a descent to bring the airspeed back up to nominal, so these angle-of-attack errors are transient and would also be averaged out to some degree by the wind estimation algorithm. The time constant of the airspeed loop is approximately 2 s, so the maximum transient horizontal wind errors caused by control system angle-of-attack variation are proportional to wind variations about nominal airspeed at the level of 9%, but these would be reduced by a factor of 3 at a scale size of 28 m, and by a factor of 7, to 1.3% at the scale size of 50 m used in the wind estimation algorithm. For example, a 5 m s^{-1} wind speed variation at a scale size of 50 m would induce a relative wind magnitude error, due to control system angle-of-attack reaction, of only 0.07 m s^{-1}.

The errors in the wind estimate as a result of GPS velocity are more difficult to bound. A "truth" reference for actual GPS velocity for the particular receiver used is problematic: receivers are rarely tested under representative conditions, and details of the internal tracking filters are held proprietary by the manufacturer. So, a definitive quantification of GPS velocity errors in flight is currently not available. Ground testing (with a stationary vehicle) produces GPS velocity errors typically below $\pm 0.05 \text{ m s}^{-1}$. Current work is seeking to measure these errors under known vehicle motions (centripetal accelerations, rotation of antenna patterns against the GPS satellites constellation, etc.) so that detailed error models can be constructed. For compatibility with the airspeed data, GPS velocity was filtered in the same way, that is, averaged over an effective 50-m scale size.

The sensitivity of wind estimates to the variation in the six data values (one relative wind magnitude and two horizontal GPS ground speed components at each pair of locations) can be quantified by examining the maximum singular values of the 2×6 Jacobian of this mapping. This describes the worst-case error in wind

estimates as a result of a given magnitude error in the data. Based on the above discussion, a 0.1 m s^{-1} error magnitude in the data is taken as representative of GPS errors and is much larger than the expected relative wind error. Resulting maximum singular values of the Jacobian are between 6 and 15 for these flights. These become larger as the two GPS velocities in the data become equal; circular motion produces smooth, constantly changing GPS velocity vectors and helps improve the condition of the solution. This implies that errors in instantaneous wind estimates can be up to $0.6–1.5 \text{ m s}^{-1}$.

REFERENCES

Balsley, B. B., M. L. Jensen, and R. Frehlich, 1998: The use of state-of-the-art kites for profiling the lower atmosphere. *Bound.-Layer Meteor.*, **87**, 1–25, https://doi.org/10.1023/A:1000812511429.

——, D. C. Fritts, R. G. Frehlich, R. M. Jones, S. L. Vadas, and R. Coulter, 2002: Up-gully flow in the great plains region: A mechanism for perturbing the nighttime lower atmosphere? *Geophys. Res. Lett.*, **29**, 1931, https://doi.org/10.1029/2002GL015435.

——, R. G. Frehlich, M. L. Jensen, Y. Meillier, and A. Muschinski, 2003: Extreme gradients in the nocturnal boundary layer: Structure, evolution, and potential causes. *J. Atmos. Sci.*, **60**, 2496–2508, https://doi.org/10.1175/1520-0469(2003)060<2496:EGITNB>2.0.CO;2.

——, ——, ——, ——, and ——, 2006: High-resolution in situ profiling through the stable boundary layer: Examination of the SBL top in terms of minimum shear, maximum stratification, and turbulence decrease. *J. Atmos. Sci.*, **63**, 1291–1307, https://doi.org/10.1175/JAS3671.1.

——, D. A. Lawrence, R. F. Woodman, and D. C. Fritts, 2012: Fine-scale characteristics of temperature, wind, and turbulence in the lower atmosphere (0-1,300 m) over the south Peruvian coast. *Bound.-Layer Meteor.* **147**, 165–178, https://doi.org/10.1007/s10546-012-9774-x.

Blumen, W., R. Banta, S. P. Burns, D. C. Fritts, R. Newsom, G. S. Poulos, and J. Sun, 2001: Turbulence statistics of a Kelvin–Helmholtz billow event observed in the night-time boundary layer during the Cooperative Atmosphere–Surface Exchange Study field program. *Dyn. Atmos. Oceans*, **34**, 189–204, https://doi.org/10.1016/S0377-0265(01)00067-7.

Clayson, C. A., and L. Kantha, 2008: On turbulence and mixing in the free atmosphere inferred from high-resolution soundings. *J. Atmos. Oceanic Technol.*, **25**, 833–852, https://doi.org/10.1175/2007JTECHA992.1.

COESA, 1976: *U.S. Standard Atmosphere, 1976.* NOAA, 227 pp.

Doran, J. C., J. D. Fast, and J. Horel, 2002: The VTMX 2000 campaign. *Bull. Amer. Meteor. Soc.*, **83**, 537–551, https://doi.org/10.1175/1520-0477(2002)083<0537:TVC>2.3.CO;2.

Eaton, F., S. A. Mclaughlin, and J. R. Hines, 1995: A new frequency-modulated continuous wave radar for studying planetary boundary layer morphology. *Radio Sci.*, **30**, 75–88, https://doi.org/10.1029/94RS01937.

Fernando, H. J. S., and Coauthors, 2015: The MATERHORN: Unraveling the mysteries of mountain weather. *Bull. Amer. Meteor. Soc.*, **96**, 1945–1967, https://doi.org/10.1175/BAMS-D-13-00131.1.

Frehlich, R., Y. Meillier, M. L. Jensen, and B. Balsley, 2003: Turbulence measurements with the CIRES tethered lifting system during CASES-99: Calibration and spectral analysis of

temperature and velocity. *J. Atmos. Sci.*, **60**, 2487–2495, https://doi.org/10.1175/1520-0469(2003)060<2487:TMWTCT>2.0.CO;2.

Fritts, D. C., and P. K. Rastogi, 1985: Convective and dynamical instabilities due to gravity wave motions in the lower and middle atmosphere: Theory and observations. *Radio Sci.*, **20**, 1247–1277, https://doi.org/10.1029/RS020i006p01247.

——, C. Bizon, J. A. Werne, and C. K. Meyer, 2003a: Layering accompanying turbulence generation due to shear instability and gravity-wave breaking. *J. Geophys. Res.*, **108**, 8452, https://doi.org/10.1029/2002JD002406.

——, C. Nappo, D. M. Riggin, B. B. Balsley, W. E. Eichenger, and R. K. Newsom, 2003b: Analysis of ducted motions in the stable nocturnal boundary layer during CASES-99. *J. Atmos. Sci.*, **60**, 2450–2472, https://doi.org/10.1175/1520-0469(2003)060<2450:AODMIT>2.0.CO;2.

——, L. Wang, and J. Werne, 2009: Gravity wave–fine structure interactions: A reservoir of small-scale and large-scale turbulence energy. *Geophys. Res. Lett.*, **36**, L19805, https://doi.org/10.1029/2009GL039501.

——, ——, and ——, 2013: Gravity wave–fine structure interactions. Part I: Influences of fine structure form and orientation on flow evolution and instability. *J. Atmos. Sci.*, **70**, 3710–3733, https://doi.org/10.1175/JAS-D-13-055.1.

——, G. Baumgarten, K. Wan, J. Werne, and T. Lund, 2014: Quantifying Kelvin-Helmholtz instability dynamics observed in noctilucent clouds: 2. Modeling and interpretation of observations. *J. Geophys. Res. Atmos.*, **119**, 9359–9375, https://doi.org/10.1002/2014JD021833.

——, L. Wang, M. A. Geller, D. A. Lawrence, J. Werne, and B. B. Balsley, 2016: Numerical modeling of multiscale dynamics at high Reynolds numbers: Instabilities, turbulence, and an assessment of Ozmidov and Thorpe scales. *J. Atmos. Sci.*, **73**, 555–578, https://doi.org/10.1175/JAS-D-14-0343.1.

Gossard, E. E., and W. H. Hooke, 1975: *Waves in the Atmosphere: Atmospheric Infrasound and Gravity Waves; Their Generation and Propagation*. Developments in Atmospheric Science, Vol. 2, Elsevier, 472 pp.

——, J. E. Gaynor, R. J. Zamora, and W. D. Neff, 1985: Fine structure of elevated stable layers observed by sounder and *in situ* tower sensors. *J. Atmos. Sci.*, **42**, 2156–2169, https://doi.org/10.1175/1520-0469(1985)042<2156:FOESLO>2.0.CO;2.

Grimshaw, R. H. J., 2002: Internal solitary waves. *Environmental Stratified Flows*, R. H. J. Grimshaw, Ed., Topics in Environmental Fluid Mechanics, Vol. 3, Springer, 1–27.

Hecht, J. H., and Coauthors, 2014: The life cycle of instability features measured from the Andes Lidar Observatory over Cerro Pachon on 24 March 2012. *J. Geophys. Res. Atmos.*, **119**, 8872–8898, https://doi.org/10.1002/2014JD021726.

Lawrence, D. A., and B. B. Balsley, 2013a: High-resolution atmospheric sensing of multiple atmospheric variables using the DataHawk small airborne measurement system. *J. Atmos. Oceanic Technol.*, **30**, 2352–2366, https://doi.org/10.1175/JTECH-D-12-00089.1.

——, and ——, 2013b: Design of a low-cost UAS for high-resolution atmospheric sensing. *Proc. AIAA InfoTech@*

Aerospace Conf., Boston, MA, AIAA, AIAA 2013-4669, https://doi.org/10.2514/6.2013-4669.

——, E. W. Frew, and W. J. Pisano, 2008: Lyapunov vector fields for autonomous UAV flight control. *J. Guid. Control Dyn.*, **31**, 1220–1229, https://doi.org/10.2514/1.34896.

Mahrt, L., 1985: Vertical structure and turbulence in the very stable boundary layer. *J. Atmos. Sci.*, **42**, 2333–2349, https://doi.org/10.1175/1520-0469(1985)042<2333:VSATIT>2.0.CO;2.

——, 1999: Stratified atmospheric boundary layers. *Bound.-Layer Meteor.*, **90**, 375–396, https://doi.org/10.1023/A:1001765727956.

Meillier, J., R. G. Frehlich, R. M. Jones, and B. B. Balsley, 2008: Modulation of small-scale turbulence by ducted waves in the nocturnal boundary layer. *J. Atmos. Sci.*, **65**, 1414–1427, https://doi.org/10.1175/2007JAS2359.1.

Muschinski, A., and C. Wode, 1998: First in situ evidence for coexisting submeter temperature and humidity sheets in the lower free troposphere. *J. Atmos. Sci.*, **55**, 2893–2906, https://doi.org/10.1175/1520-0469(1998)055<2893:FISEFC>2.0.CO;2.

——, P. B. Chilson, S. Kern, J. Nielinger, G. Schmidt, and T. Prenosil, 1999: First frequency-domain interferometry observations of large-scale vertical motion in the atmosphere. *J. Atmos. Sci.*, **56**, 1248–1258, https://doi.org/10.1175/1520-0469(1999)056<1248:FFDIOO>2.0.CO;2.

Nappo, C. J., 2013: *An Introduction to Atmospheric Gravity Waves*. International Geophysics Series, Vol. 102, Academic Press, 359 pp.

Newsom, R. K., and R. M. Banta, 2003: Shear-flow instability in the stable nocturnal boundary layer as observed by Doppler lidar during CASES-99. *J. Atmos. Sci.*, **60**, 16–33, https://doi.org/10.1175/1520-0469(2003)060<0016:SFIITS>2.0.CO;2.

Poulos, G. S., and Coauthors, 2002: CASES-99: A comprehensive investigation of the stable nocturnal boundary layer. *Bull. Amer. Meteor. Soc.*, **83**, 555–581, https://doi.org/10.1175/1520-0477(2002)083<0555:CACIOT>2.3.CO;2.

Sorbjan, Z., and B. B. Balsley, 2008: Microstructure of turbulence in the stably stratified boundary layer. *Bound.-Layer Meteor.*, **129**, 191–210, https://doi.org/10.1007/s10546-008-9310-1.

Stull, R. B., 2012: *An Introduction to Boundary Layer Meteorology*. Springer, 670 pp.

Sun, J., S. P. Burns, D. H. Lenschow, R. Banta, and R. Newsom, 2002: Intermittent turbulence associated with a density current passage in the stable boundary layer. *Bound.-Layer Meteor.*, **105**, 199–219, https://doi.org/10.1023/A:1019969131774.

——, D. H. Lenschow, and S. P. Burns, 2004: Atmospheric disturbances that generate intermittent turbulence in nocturnal boundary layers. *Bound.-Layer Meteor.*, **110**, 255–279, https://doi.org/10.1023/A:1026097926169.

Thorpe, S. A., 1977: Turbulence and mixing in a Scottish loch. *Philos. Trans. Roy. Soc. London*, **A286**, 125–181, https://doi.org/10.1098/rsta.1977.0112.

Whiteman, C. D., and Coauthors, 2008: METCRAX 2006: Meteorological experiments in Arizona's Meteor Crater. *Bull. Amer. Meteor. Soc.*, **89**, 1665–1681, https://doi.org/10.1175/2008BAMS2574.1.